



HAWC+ Far-infrared Observations of the Magnetic Field Geometry in M51 and NGC 891

Terry Jay Jones¹ , Jin-Ah Kim¹ , C. Darren Dowell² , Mark R. Morris³ , Jorge L. Pineda⁴ , Dominic J. Benford⁵ , Marc Berthoud^{6,7} , David T. Chuss⁸ , Daniel A. Dale⁹ , L. M. Fissel¹⁰ , Paul F. Goldsmith² , Ryan T. Hamilton¹¹ , Shaul Hanany¹² , Doyal A. Harper¹³ , Thomas K. Henning¹⁴ , Alex Lazarian¹⁵ , Leslie W. Looney¹⁶ , Joseph M. Michail^{7,8,17} , Giles Novak⁷ , Fabio P. Santos^{7,18} , Kartik Sheth¹⁹ , Javad Siah⁸ , Gordon J. Stacey²⁰ , Johannes Staguhn^{21,22} , Ian W. Stephens²³ , Konstantinos Tassis^{24,25} , Christopher Q. Trinh²⁶ , John E. Vaillancourt^{27,28,30} , Derek Ward-Thompson²⁹ , Michael Werner² , Edward J. Wollack²² , and Ellen G. Zweibel¹⁵

(HAWC+ Science Team)

¹ Minnesota Institute for Astrophysics, University of Minnesota, Minneapolis, MN 55455, USA; tjj@astro.umn.edu

² NASA Jet Propulsion Laboratory, California Institute of Technology, 4800 Oak Grove Drive, Pasadena, CA 91109, USA

³ Department of Physics and Astronomy, University of California, Los Angeles, Box 951547, Los Angeles, CA 90095-1547, USA

⁴ Jet Propulsion Laboratory, California Institute of Technology, 4800 Oak Grove Drive, Pasadena, CA 91109, USA

⁵ NASA Headquarters, 300 E Street SW, Washington, DC 20546, USA

⁶ Engineering + Technical Support Group, University of Chicago, Chicago, IL 60637, USA

⁷ Center for Interdisciplinary Exploration and Research in Astrophysics (CIERA), and Department of Physics & Astronomy, Northwestern University, 2145 Sheridan Road, Evanston, IL 60208, USA

⁸ Department of Physics, Villanova University, 800 E Lancaster Avenue, Villanova, PA 19085, USA

⁹ Department of Physics & Astronomy, University of Wyoming, Laramie, WY, USA

¹⁰ Department of Physics, Engineering Physics and Astronomy, Queen's University, 64 Bader Lane, Kingston, ON K7L 3N6, Canada

¹¹ Lowell Observatory, 1400 W Mars Hill Road, Flagstaff, AZ 86001, USA

¹² School of Physics and Astronomy, University of Minnesota/Twin Cities, Minneapolis, MN 55455, USA

¹³ Department of Astronomy and Astrophysics, University of Chicago, Chicago, IL 60637, USA

¹⁴ Max Planck Institute for Astronomy, Königstuhl 17, D-69117 Heidelberg, Germany

¹⁵ Department of Astronomy, University of Wisconsin, Madison, WI 53706, USA

¹⁶ Department of Astronomy, University of Illinois, 1002 West Green Street, Urbana, IL 61801, USA

¹⁷ Department of Astrophysics and Planetary Science, Villanova University, 800 E Lancaster Avenue, Villanova, PA 19085, USA

¹⁸ Max-Planck-Institute for Astronomy, Königstuhl 17, D-69117 Heidelberg, Germany

¹⁹ NASA Headquarters, 300 E Street SW, DC 20546, USA

²⁰ Department of Astronomy, Cornell University, Ithaca, NY 14853, USA

²¹ Dept. of Physics & Astronomy, Johns Hopkins University, Baltimore, MD 21218, USA

²² NASA Goddard Space Flight Center, Greenbelt, MD 20771, USA

²³ Center for Astrophysics, Harvard & Smithsonian, 60 Garden Street, Cambridge, MA, USA

²⁴ Department of Physics and ITCF, University of Crete, GR-70013 Heraklion, Greece

²⁵ Institute of Astrophysics, Foundation for Research and Technology-Hellas, Vassilika Vouton, GR-70013 Heraklion, Greece

²⁶ USRA/SOFIA, NASA Armstrong Flight Research Center, Building 703, Palmdale, CA 93550, USA

²⁷ Universities Space Research Association, NASA Ames Research Center, Moffett Field, CA 94035, USA

²⁸ Enrico Fermi Institute, Department of Astronomy and Astrophysics, University of Chicago, Chicago, IL 60637, USA

²⁹ Jeremiah Horrocks Institute, University of Central Lancashire, Preston PR1 2HE, UK

Received 2020 June 17; revised 2020 July 22; accepted 2020 August 6; published 2020 September 21

Abstract

Stratospheric Observatory for Infrared Astronomy High-resolution Airborne Wideband Camera Plus polarimetry at $154\ \mu\text{m}$ is reported for the face-on galaxy M51 and the edge-on galaxy NGC 891. For M51, the polarization vectors generally follow the spiral pattern defined by the molecular gas distribution, the far-infrared (FIR) intensity contours, and other tracers of star formation. The fractional polarization is much lower in the FIR-bright central regions than in the outer regions, and we rule out loss of grain alignment and variations in magnetic field strength as causes. When compared with existing synchrotron observations, which sample different regions with different weighting, we find the net position angles are strongly correlated, the fractional polarizations are moderately correlated, but the polarized intensities are uncorrelated. We argue that the low fractional polarization in the central regions must be due to significant numbers of highly turbulent segments across the beam and along lines of sight in the beam in the central 3 kpc of M51. For NGC 891, the FIR polarization vectors within an intensity contour of $1500\ \text{MJy sr}^{-1}$ are oriented very close to the plane of the galaxy. The FIR polarimetry is probably sampling the magnetic field geometry in NGC 891 much deeper into the disk than is possible with NIR polarimetry and radio synchrotron measurements. In some locations in NGC 891, the FIR polarization is very low, suggesting we are

preferentially viewing the magnetic field mostly along the line of sight, down the length of embedded spiral arms. There is tentative evidence for a vertical field in the polarized emission off the plane of the disk.

Unified Astronomy Thesaurus concepts: Disk galaxies (391); Galaxy magnetic fields (604)

³⁰ Current address: Lincoln Laboratory, Massachusetts Institute of Technology, Lexington, MA 02421-6426, USA.



Original content from this work may be used under the terms of the [Creative Commons Attribution 4.0 licence](https://creativecommons.org/licenses/by/4.0/). Any further distribution of this work must maintain attribution to the author(s) and the title of the work, journal citation and DOI.

1. Introduction

A face-on and an edge-on galaxy each provides the observer with a unique advantage that enhances the study of the properties of spiral galaxies in general. For a face-on galaxy, there is far less confusion caused by multiple sources along the line of sight, a minimum column density of gas, dust and cosmic-ray electrons, and a clear view of spiral structure. For an edge-on galaxy, the vertical structure of the disk is easily discernible, vertical outflows and super-bubbles can be seen, and the fainter, more diffuse halo is now more accessible. M51 and NGC 891 provide two well-studied examples of nearly face-on (M51) and edge-on (NGC 891) galaxies. We are interested in probing the magnetic field geometry in these two systems to compare far-infrared (FIR) observations with optical, near-infrared (NIR) and radio observations, and to search for clues to the mechanism(s) for generating and sustaining magnetic fields in spiral galaxies.

Over the past few decades, astronomers have detected magnetic fields in galaxies at many spatial scales. These studies have been performed using optical, NIR, CO, and radio observations (see Kronberg 1994; Zweibel & Heiles 1997; Jones 2000; Beck & Gaensler 2004; Li & Henning 2011; Montgomery & Clemens 2014; Beck 2015, for example). In most nearly face-on spirals, synchrotron observations reveal a spiral pattern to the magnetic field, even in the absence of a clear spiral pattern in the surface brightness (Beck & Gaensler 2004; Fletcher 2010). If magnetic fields are strongly tied to the orbital motion of the gas and stars, differential rotation would quickly wind them up and produce very small pitch angles. The fact that this is clearly not the case is an argument in favor of a decoupling of the magnetic field geometry from the gas flow due to diffusion of the field (Beck & Wielebinski 2013), which is expected in highly conductive interstellar medium (ISM) environments (e.g., Lazarian et al. 2012).

Radio observations measure the polarization of centimeter wave synchrotron radiation from relativistic electrons, which is sensitive to the cosmic-ray electron density and magnetic field strength (Jones et al. 1974; Beck 2015). Li & Henning (2011) measured the magnetic field geometry in several star-forming regions in M33 by observing CO emission lines polarized due to the Goldreich–Kylafis effect (Goldreich & Kylafis 1981), although there is an inherent 90° ambiguity in the position angle with this technique. Studies of interstellar polarization using the transmission of starlight at optical and NIR wavelengths can reveal the magnetic field geometry as a result of dichroic extinction by dust grains aligned with respect to the magnetic field (e.g., Jones & Whittet 2015) where the asymmetric dust grains are probably aligned by radiative alignment torques (Lazarian & Hoang 2007; Andersson et al. 2015). However, polarimetric studies at these short wavelengths of diffuse sources such as galaxies can be affected by contamination from highly polarized, scattered starlight. This light originates with stars in the disk and the bulge that subsequently scatters off dust grains in the interstellar medium (Jones et al. 2012). The optical polarimetry vector map of M51 (Scarrott et al. 1987) was claimed to trace the interstellar polarization in extinction and does indeed follow the spiral pattern. As we will see later in the paper, it also demonstrates a remarkable degree of agreement with our High-resolution Airborne Wideband Camera Plus (HAWC+) map of the

magnetic field geometry. A more recent upper limit to the polarization measured at NIR wavelengths appeared to rule out dichroic extinction of starlight as the main polarization mechanism (Pavel & Clemens 2012). The scattering cross section of normal interstellar dust declines much faster ($\sim \lambda^{-4}$ between 0.55 and 1.65 μm) than its absorption, which goes as $\sim \lambda^{-1}$ (Jones & Whittet 2015). It is therefore possible that the optical polarization measured by Scarrott et al. (1987) is due to scattering, rather than extinction by dust grains aligned with the interstellar magnetic field, since polarimetric studies at these short wavelengths of diffuse sources such as galaxies can be affected by contamination from highly polarized scattered light (Wood & Jones 1997; Seon 2018). Nevertheless, the similarity we will find between the optical data and FIR results is striking, but if they are both indicating the same magnetic field, then the non-detection in the NIR is a mystery. Note that we will find a similar dilemma in comparing the optical and FIR polarimetry of NGC 891.

Observing polarization at FIR wavelengths has some advantages over, and is very complementary to, observations at optical, NIR, and radio centimeter wavelengths for the following reasons: (1) The dust is being detected in polarized thermal emission from elongated grains oriented by the local magnetic field (see the review by Jones & Whittet 2015), not extinction of a background source, as is the case at optical and NIR wavelengths. (2) Scattering is not a contaminant since the wavelength is much larger than the grains, and much higher column densities along the line of sight can be probed. (3) Faraday rotation—which is proportional to λ^2 , must be removed from radio synchrotron observations, and can vary across the beam—is insignificant for our FIR polarimetry (Kraus 1966). (4) The inferred magnetic field geometry probed by FIR polarimetry is weighted by dust column depth and dust grain temperature, not cosmic-ray density and magnetic field strength, as is the case for synchrotron emission. In this paper we report observations at 154 μm of both M51 and NGC 891 using HAWC+ on the Stratospheric Observatory for Infrared Astronomy (SOFIA; Harper et al. 2018) with FWHM beam sizes of 560 and 550 pc, respectively. In all cases, we have rotated the FIR polarization vectors by 90° to indicate the implied magnetic field direction. This rotation is also made for synchrotron emission at radio wavelengths, but is *not* made for optical and NIR polarimetry where the polarization is caused by extinction (unless contaminated by scattering), not emission, and directly delineates the magnetic field direction. The polarization position angles are not true vectors indicating a single direction, but the term “vector” has such a long historical use that we will use that term here to describe the position angle and magnitude of a fractional polarization at a location on the sky. The polarization is a true vector in a Q , U , or Q/I , U/I diagram, but this translates to a 180° duplication on the sky.

2. Far-infrared Polarimetric Observations

The 154 μm HAWC+ observations presented in this paper were acquired as part of SOFIA Guaranteed Time Observation program 70_0609 and Director’s Discretionary Time program 76_0003. The HAWC+ imaging and polarimetry—resulting in maps of continuum Stokes I , Q , U —used the standard nod match chop (NMC) observing mode, performed at four half-wave plate angles and sets of four dither positions. Multiple

dither size scales were used in order to even the coverage in the center of the maps.

The M51 data were acquired during two flight series, on SOFIA flights 450, 452, and 454 in 2017 November and on flights 545 and 547 in 2019 February. The chop throw for the 2017 November observations was 6.7 at a position angle of 105° east of north. For the 2019 February observations, the chop throw was 7.5 in the east–west direction. The total elapsed time for the M51 observations was 4.6 hr. The observations with telescope elevation $>58^\circ$ at the end of flight 547 were discarded due to vignetting by the observatory door. Otherwise, conditions were nominal.

The NGC 891 data were acquired on flight 450 and on flights 506 and 510 in 2018 September. The chop throw for all observations was 5.0 at a position angle of 115° east of north. The total elapsed time for the NGC 891 observations was 3.2 hr. Four dither positions with telescope tracking problems during flight 450 (which did not successfully run through the data analysis pipeline) were discarded. Otherwise, observing conditions were nominal.

2.1. Data Reduction

All HAWC+ imaging and polarimetry were reduced with HAWC+ data reduction pipeline 1.3.0beta3 (2018 April). Following standard pipeline practice, we subtracted an instrumental polarization $\{q_i, u_i\}$, calibrated with separate “skydip” observations, having a median value of $\sqrt{q_i^2 + u_i^2}$ of 2.0% over the detector array. The final uncertainties were increased uniformly by $\sim 30\%$ – 40% based on the χ^2 consistency check described by Santos et al. (2019). We applied map-based de-glitching as described by Chuss et al. (2019). Due to smoothing with a kernel approximately half the linear size of the beam, the angular resolution in the maps (based on Gaussian fits) is $14''$ FWHM at $154\ \mu\text{m}$. Since both galaxies are well out of the Galactic plane, reference beam contamination is minimized.

The flux densities in the maps were calibrated using observations of solar system objects, also in NMC mode. Due to the lack of a reliable, calibrated SOFIA facility water vapor monitor at the time of the observations, the version 1.3.0 pipeline uses an estimate of far-IR atmospheric absorption that is dependent on observatory altitude and telescope elevation, but is constant in time. For all observations, we used the default pipeline flux calibration factor, for which we estimate 20% absolute uncertainty. For each galaxy, the maps from the two flight series, analyzed separately, show flux calibration consistency to within 5%. For M51, we adjusted the coordinates of the 2019 February map (with a simple translation in both axes) prior to coaddition with the 2017 November map. The relative alignment of the per-flight-series maps for NGC 891 was within a fraction of a beam without adjustment.

Alignment of the coordinate system for M51 supplied by the pipeline was checked against Very Large Array (VLA) 3.6, 6.2, and 20.5 cm (Fletcher et al. 2011), Spitzer $8\ \mu\text{m}$ (Smith et al. 2007), and Herschel $160\ \mu\text{m}$ maps (Pilbratt et al. 2010). We did this by matching six small, high surface brightness regions between our $154\ \mu\text{m}$ map and the maps at the other wavelengths. We found that the HAWC+ map was consistently $4'' \pm 1''$ south relative to the comparison maps. For this reason, we have added an offset of $4''$ north to our maps of M51. Since we are not making any comparisons of NGC 891

with high-resolution maps at other wavelengths, we made no adjustment to the coordinate system for that galaxy.

2.2. Polarimetry Analysis

For both galaxies, we computed the net polarization in different synthetic aperture sizes, depending on the signal-to-noise ratio (S/N) in the data. The pixel size is $3.4''$, or $\sim 1/4$ an FWHM beamwidth. In all cases we used the I , Q , and U intensity and error maps to form the polarization vectors. The results reported here were obtained by placing different sized synthetic apertures on the images and computing intensities from the sums of individual pixels and the errors from the sums of the error images in that aperture in quadrature. The errors and intensities in the individual pixels are not statistically independent, since they were created by combining intermediate images in the data processing and then smoothed with a truncated Gaussian with FWHM = 2.04 pixels ($6.93''$). We determined the effect of the Gaussian kernel on the computed errors by applying it to maps with random noise. As a result of this exercise, we increased the computed error by factors of 1.69 for the 2×2 pixel (half beam), 2.27 for the 4×4 pixel (one beam), and 2.56 for the 8×8 pixel (two beam) synthetic apertures.

An additional concern is spatially correlated noise such as might be due to incomplete subtraction of atmospheric noise and other effects. A thorough investigation into the possibility of correlated noise in our data is beyond the scope of this paper and will be addressed in a later paper, but we report the results of a simple test for spatially correlated noise carried out by the HAWC+ instrument team (Fabio P. Santos) in 2017 on B and C observations of HL Tau. This analysis showed that an approximate quadrupling of the sky area causes the noise in the data (compared to what would be expected from uncorrelated noise) to be increased by a factor of 1.06. Specifically, results were compared for a Gaussian smoothing kernel of $4''$ FWHM truncated at an $8''$ diameter and one having $7.8''$ FWHM with truncation at a $15.6''$ diameter.

For this reason we have made extra cuts in Stokes I (total intensity) at an S/N of 50:1 for M51 and 30:1 for NGC 891, and increased the error for the largest synthetic aperture of 8×8 pixels by a factor of 1.06. We are particularly concerned about the scientifically important inter-arm and halo regions, which have low intensity and need to use the larger synthetic aperture. Q and U are *intensities*, and small spurious values will adversely influence the net polarization derived for regions of low intensity, but not high intensity. For example, at a contour level of $100\ \text{MJy sr}^{-1}$ between the arms, a $1\ \text{MJy sr}^{-1}$ value for Q that is due to a glitch, a bad pixel, or residual flux from image subtraction will produce a 1% polarization that is not real. In the arm where the intensity is $\sim 800\ \text{MJy sr}^{-1}$, this would contribute no more than 0.12%. The final computed polarization was then corrected for polarization bias (Wardle & Kronberg 1974; Sparks & Axon 1999), and cuts were made at a fractional polarization for a final S/N of $\geq 3:1$ and S/N between 2.5:1 and 3:1.

To further guard against systematic errors in the I , Q , and U maps at lower intensities, we made a cut using the total intensity error I_{err} map at $\sigma > 0.003\ \text{Jy pixel}^{-1}$. This removed the outer regions of the images where there was incomplete overlap in the dithered images. This final cut made little difference in the M51 polarimetry results where less than 10% of the image was removed. But, for NGC 891, about 20% of

the image was removed, and the northern and southern extremes of the disk in NGC 891 were excluded. Note that the edge-on disk in NGC 891 is at least $10'$ long, and our HAWC+ image spans only about $5'$ along the disk, centered on the nucleus. In an upcoming paper, we will be working with existing and new HAWC+ data on M51 and will create smoothed images starting with the raw data.

3. M51

3.1. Introduction

M51 is not only a face-on spiral galaxy but also a two-arm, grand design spiral (e.g., Rand et al. 1992), at a distance of 8.5 Mpc (McQuinn et al. 2016). It is clearly interacting with M51b, and tails and bridges in the outer regions of the two galaxies are shared, while in the inner regions of M51, the spiral structure appears to be unaffected by the companion. Our observations did not reach far enough from the center of the galaxy to include M51b. Because of its low inclination, M51 shows well-defined spiral arms and separated arm and inter-arm regions. This makes M51 an excellent laboratory to study how the magnetic field geometry changes from arm to inter-arm regions due to the effect of spiral density waves and turbulence. Star formation in M51 is located mostly in the spiral arms and in the central region, but some gas and star formation are also detected in the inter-arm regions (e.g., Koda et al. 2009). Molecular gas is strongly correlated with the optical and infrared spiral arms and shows evidence for spurs in the gas distribution (Schinnerer et al. 2017). The magnetic field geometry of M51 was studied at radio wavelengths by Fletcher et al. (2011), who found that the overall geometry revealed in the polarization vectors follows the spiral pattern, but there is depolarization in their larger $15'' \times 20.5$ cm beam. They found that the 6.2 cm polarized emission is probably strongly affected by sub-beam-scale anisotropies in the field geometry. Our HAWC+ observations allow us to study the magnetic field geometry as measured by dust emission instead of cosmic-ray electrons, and thereby sample the line of sight differently, and also probe denser components of the ISM than is possible at optical and NIR wavelengths.

3.2. Magnetic Field Geometry

The polarization vector map of M51 is shown in Figure 1, where the polarization vectors have been rotated 90° to show the inferred magnetic field geometry. Fractional polarization values range from a high of 9% to a low of 0.6%, about 3σ above our estimated limiting fractional polarization of 0.2% (Jones et al. 2019). Clearly evident in Figure 1 is a strong correlation between the position angles of the FIR polarimetry and the underlying spiral arm pattern seen in the color map. This can be better visualized in Figure 2, where all of the polarization vector lengths have been set to unity, and only the position angle is quantified.

In spiral galaxies, the spiral pattern is often fitted with a logarithmic spiral (e.g., Seigar & James 1998; Davis et al. 2012), a mathematical curve that is characterized by a constant pitch angle. The pitch angle is an empirical parameter that quantifies the morphology of galaxies regardless of their distance. Pitch angles for the spiral features in M51 have been investigated at different wavelengths and using different methods. Shetty et al. (2007) found a pitch angle of 21.1° for the bright CO emission in the spiral arms. Hu et al. (2013)

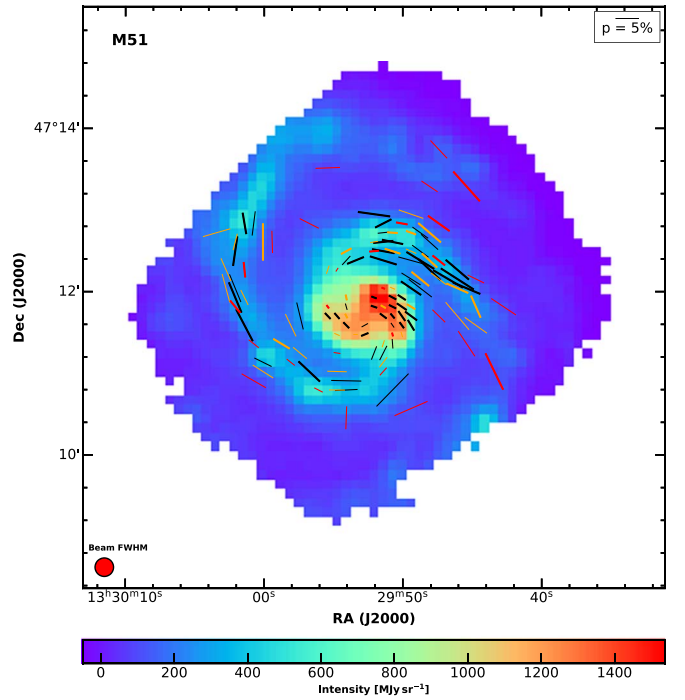


Figure 1. Fractional polarization vector map of M51 at a wavelength of $154 \mu\text{m}$, with the vectors rotated 90° to represent the inferred magnetic field direction. Data points using a square $6''8 \times 6''8$ “half” beam are plotted in black. Data points using a $13''6 \times 13''6$ “full” beam are plotted in orange, and red vectors are computed using a $27''2 \times 27''2$ square beam. The red disk in the lower left corner indicates the FWHM footprint of the HAWC+ beam on the sky at $154 \mu\text{m}$. Colors in the underlying image define the $154 \mu\text{m}$ continuum intensity. Vectors with $S/N \geq 3:1$ have thick lines, and vectors with S/N from 2.5:1 to 3:1 have thin lines.

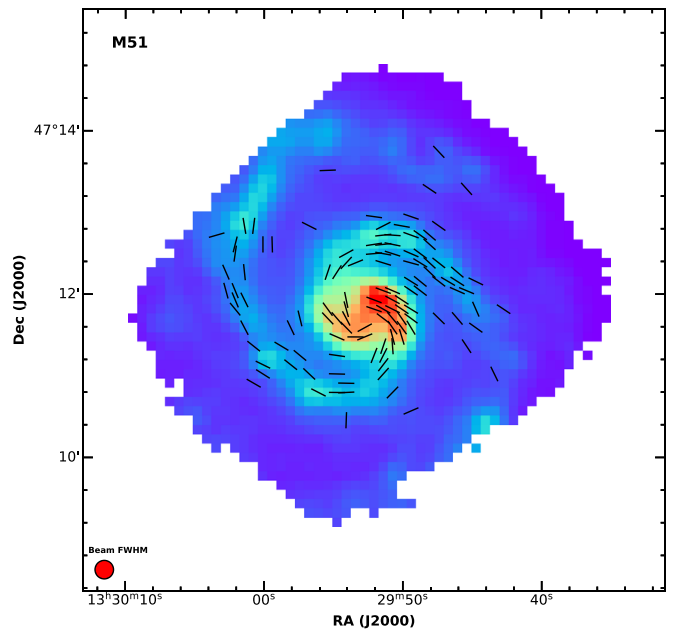


Figure 2. Same as Figure 1, except all of the polarization vectors have been set to the same length and color to better illustrate their position angles.

suggested 17.1° and 17.5° for each of the two arms using SDSS images, and Puerari et al. (2014) found a pitch angle of 19° for the arms from $8 \mu\text{m}$ images. Also, several investigators found that the pitch angles are variable depending on the location

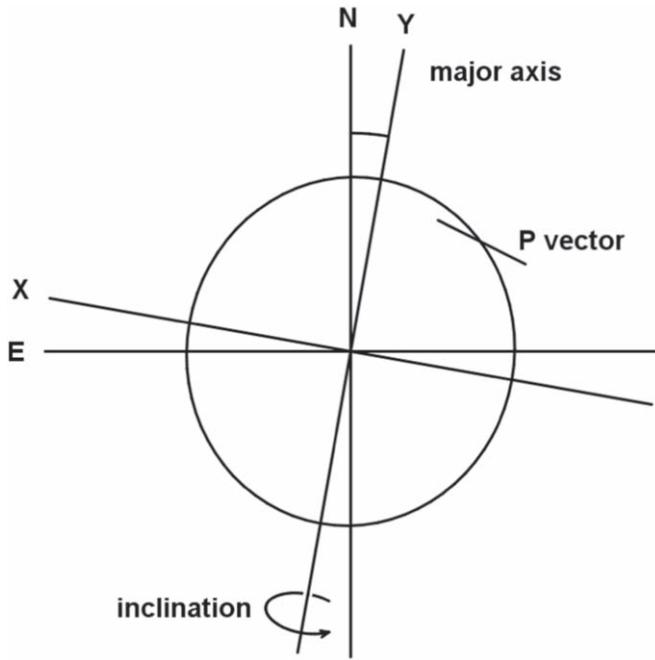


Figure 3. Geometry used to de-project the polarization vectors so that their individual pitch angles can be calculated. The inclination with respect to the plane of the sky is 20° , and the major axis (labeled “Y”) of the ellipse (a circle in projection) is 170° east of north. We are assuming the magnetic field vectors in the disk of M51 have *no* vertical component when computing the de-projection. The polarization vector is shown relative to a circle (in projection), which has a pitch angle of zero.

(e.g., Howard & Byrd 1990; Patrikeev et al. 2006; Puerari et al. 2014).

M51 is not perfectly face-on, but rather is tilted to the line of sight. Shetty et al. (2007) used the values for the inclination of 20° and a position angle for the major axis of 170° from Tully (1974) in their analysis of the spiral arms seen in CO emission. This geometry is illustrated in Figure 3. Using these same parameters and assuming that the intrinsic magnetic field vector has *no* component perpendicular to the disk, we can de-project our vectors and compute their individual pitch angles using the geometry from Figure 3 (see Lopez-Rodriguez et al. 2020). Having de-projected our vectors, we can compare the pitch angles of our vectors with the pitch angle(s) of a model spiral where we compute $\Delta\theta = \text{PA}_{\text{FIR}} - \text{PA}_{\text{spiral}}$ where PA indicates pitch angle for the (de-projected) FIR polarimetry vectors and the model spiral, respectively.

First, we assume a single pitch angle of $21^\circ.1$ from the CO observations for the model spiral arms, and compute $\Delta\theta$. We will call this Model 1. A normalized histogram of $\Delta\theta$ is shown in Figure 4. We simulated the expected distribution in $\Delta\theta$ under the assumption that the vectors and the spiral arm pitch angle were the same, and only errors in the FIR polarization data were responsible for the dispersion in the angle difference. We generated simulated data assuming the errors in polarization position angle are Gaussian distributed for each vector, and we ran a Monte Carlo routine that generated simulated distributions, repeated 1000 times. Since the simulated data are assumed to follow the arm exactly, the peak of the distribution function is set at $\Delta\theta = 0$. When the observational data and simulation are compared, the distribution of observed $\Delta\theta$ is broader than the simulated one with a standard deviation of $\sigma = 23^\circ$ compared to $\sigma = 9^\circ$ for the simulation. The observational data shows greater departure from a single pitch

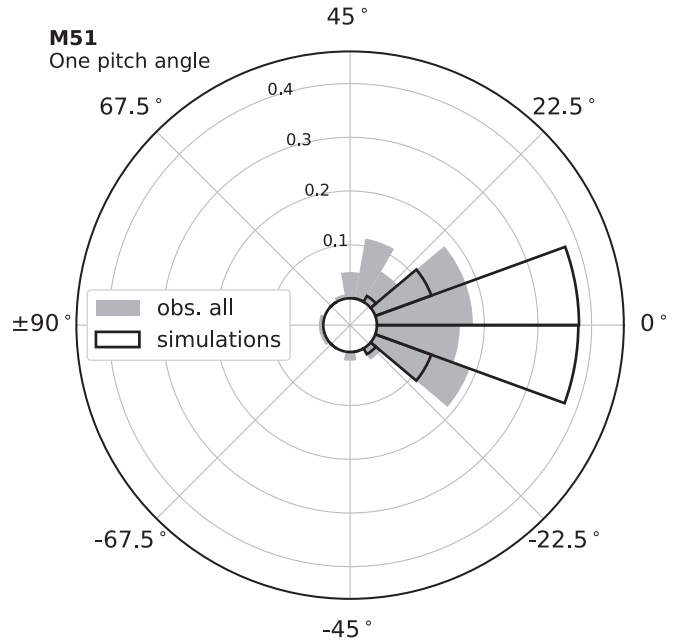


Figure 4. Histogram distribution of $\Delta\theta$ between the pitch angle of our polarization vectors and a single pitch angle for the spiral arms of $21^\circ.1$ (Model 1). Radial distance is the fraction of the total number of measurements. The area in gray shows the actual data, and the solid lines show a simulation (see the text) under the assumption that the pitch angles are intrinsically the same, and only errors in the data contribute to the dispersion.

angle than can be accounted for by errors in the FIR polarimetry vector position angles alone.

Next we modeled the spiral features with two pitch angles, with a change in pitch angle chosen to fit the FIR intensity data by eye. We will call this Model 2. The resulting model spiral arms are shown in Figure 5 where the inner spiral arms at a radial distance of $137''$ from the center retain the $21^\circ.1$ pitch angle based on the CO observations for part of the arms, and then a much tighter pitch angle of $3^\circ.9$ is used for the outer arms. Following the same procedure as before, we computed the angle difference between the pitch angles of the polarization vectors and the spiral arms and ran a simulation of these differences, assuming they are intrinsically the same, and only observational errors are responsible for the dispersion in the differences. For this two-pitch-angle case, the results are plotted in Figure 6. Even with the two-pitch-angle model, the dispersion in $\Delta\theta$ is much greater than can be accounted for by the observational errors with nearly identical standard deviations to Model 1. To explore the spiral pattern in our polarimetry vectors in more detail, we separated the magnetic field vectors into arm, inter-arm, and central regions. These regions are classified according to the mask given in Figure 1 of Pineda et al. (2018), where the central region is roughly the inner 3 kpc (in diameter). Note that we are interpolating both models into the inter-arm region (see the blue line in Figure 5). The distribution of $\Delta\theta$ for these separate regions is shown in the right panel of Figure 6. The vectors in the center group have a distinct positive mean offset of $17^\circ.4$, which means a more open spiral pattern compared to the model pitch angle. The inter-arm and arm groups have no clear offset from zero, but the dispersion is still much larger than can be explained by measurement errors alone.

In Figure 5 we define ϕ , a measure of the angular distance along a spiral feature, increasing from zero clockwise around

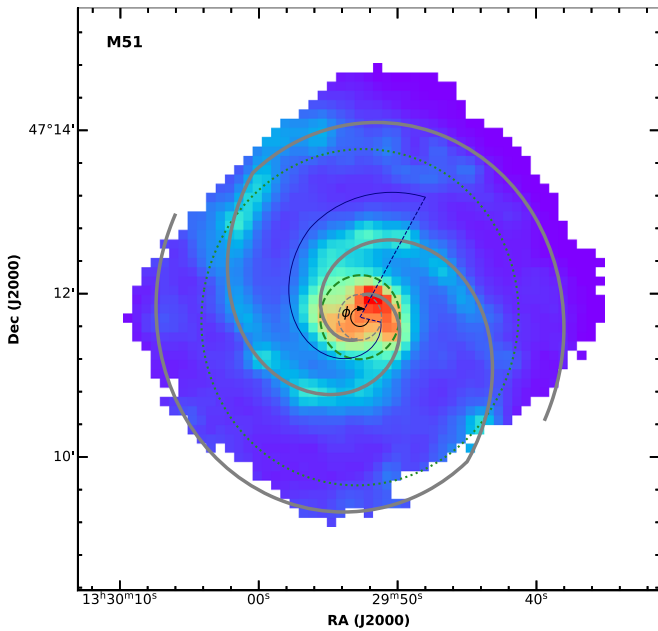


Figure 5. Model 2 geometry using two spiral arm pitch angles (shown in gray) that we used to compute the distribution of $\Delta\theta$ for this case. The inner part has the pitch angle of 21° , and the outer part a pitch angle of 3° . The green dashed and dotted lines are the inner resonance and the corotation radii, respectively, described in Tully (1974). The angle ϕ is used to define a measure of distance along a spiral “feature.” That is, we assume the basic two-pitch-angle model (shown in gray) extends between the arms (shown in blue).

the galaxy (along the spiral features). We define a spiral feature for each point in the map (see Figure 5), and extrapolate back to the central region to determine the angular distance ϕ . The pitch angle, averaged over intervals of $\phi = 40^\circ$, as a function of angular distance along a spiral model line, is illustrated in Figure 7. The top panel is the pitch angle of the FIR polarization vectors. The middle panel plots $\Delta\theta$, the difference between Model 2 and the observed pitch angles. The lower panel shows the trend in fractional polarization with ϕ . We find no statistically significant difference in the trends of fractional polarization with ϕ when comparing the arm and inter-arm regions. The dispersion for $\Delta\theta$ in the inter-arm region is large, and departs from the trend seen in the arm in the last data bin.

Overall our FIR vectors follow the spiral arms in M51, but with fluctuations about the spiral arm direction that are greater than can be explained by measurement errors alone. Stephens et al. (2011) found no correlation between the magnetic field geometry in dense molecular clouds in the Milky Way and Galactic coordinates, and this may add a random component to the net position angles we are measuring in our large 560 pc beam. However, the relative contributions of emission from dense ($n_H > 100 \text{ cm}^{-3}$) and more diffuse regions in M51 to our $154 \mu\text{m}$ flux has not been modeled. The FIR vectors in the central region indicate a more open spiral pattern than that seen in the molecular gas (Shetty et al. 2007), opposite to what one would expect if the magnetic fields were wound up with rotation. Although our data in the inter-arm region are relatively sparse, the fractional polarization is statistically similar to the that in the arms, which are delineated by a higher FIR surface brightness.

Houde et al. (2013) used the position angle structure function (Kobulnicky et al. 1994; Hildebrand et al. 2009; Houde et al. 2016) to characterize the magnetic turbulence in M51 using the radio polarization data from Fletcher et al. (2011). See

Section 3.4 for a comparison with the radio data. Analyzing the galaxy as a whole and using a 2D Gaussian characterization of the random component to the magnetic field, they found that the turbulent correlation scale length parallel to the mean field was 98 ± 5 pc and the scale length perpendicular to the mean field was 53 ± 3 pc. This indicates that the random component has an anisotropy with respect to the spiral pattern, and could be interpreted as due to shocks in the spiral arms (Pineda et al. 2020) compressing anisotropic turbulence in a particular direction (Beck & Wielebinski 2013). We will explore the position angle structure function in a later paper with new SOFIA/HAWC+ observations that will allow us to measure fainter regions due to increased integration time.

Houde et al. (2013) also found that the ratio of random to ordered strengths of the magnetic field was tightly constrained to $B_r/B_o = 1.01 \pm 0.04$, and this ratio is consistent with other work (e.g., Jones et al. 1992; Miville-Deschênes et al. 2008). Assuming the spiral pattern represents the geometry of the ordered component, the addition of a random component may explain our broad distribution of position angles with respect to the spiral structure. Broadening of the distribution of $\Delta\theta$ by a random component depends on the number of turbulent segments in our beam. If we use the 100 pc turbulent correlation scale determined by Houde et al. (2013), there are >25 segments in our beam, which will largely “average out” relative to the ordered component (see Figure 8 in Jones et al. 1992). A simple broadening of the distribution due to this spatially small random component would not produce the number of position angles differing by 60° – 90° from the spiral pattern seen in Figure 6. However, all of the vectors that depart by more than 60° are in the inter-arm region and have S/N only between 2.5:1 and 3:1. The distribution of $\Delta\theta$ for the arm region (only) is much more similar to the simulation, with a mean value of only 5° . The dispersion, however, is still a factor of two greater. Given the uncertainty in the contribution of a random component to the magnetic field, the FIR vectors in the arms (blue bars in Figure 6) could be consistent with the spiral pattern we defined in Figure 5. But without a better estimate of the turbulent component, we cannot make a better determination. Even with these uncertainties, there remains a clear shift in the mean pitch angle for the central region to a more open (greater pitch angle) pattern than that seen in the CO and star formation tracers. More sensitive observations, in particular for the inter-arm region, will be necessary to better define the correlation between the FIR vectors and the spiral pattern.

Using broadband 20 cm observations with the VLA, Mao et al. (2015) studied the rotation measures in M51 in detail. They found that at 20 cm, most of the observations are consistent with an external uniform screen (halo) in front of the synchrotron emitting disk. The disk itself produces synchrotron emission that is partially depolarized on scales smaller than 560 pc (which is our beam size), with most of the polarized flux originating in the top layer of the disk, then passing through the halo. The scale length for the rotation measure structure function in the halo is 1 kpc, which is consistent with blowouts and super-bubbles from activity in the disk. Our FIR observations are tied to the warm dust in the disk and are largely insensitive to the magnetic field geometry in the halo, but should be sensitive to the formation of super-bubbles, which have their origin in the disk. We will be exploring the position angle pattern in more detail in a later paper.

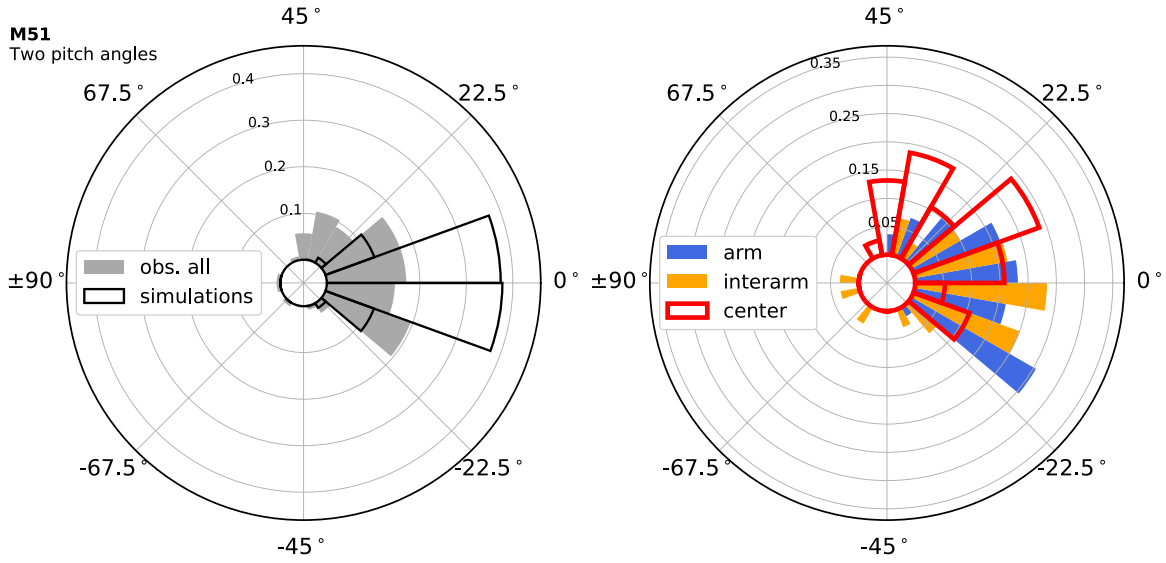


Figure 6. Distribution of $\Delta\theta$ as in Figure 4, but using Model 2, which has two pitch angles. Gray and black represent the simulation and observations, respectively. In the right panel, the observation is subdivided into arm, inter-arm, and central regions (see the text), which are indicated by blue, orange, and red, respectively. The locations of the different regions are defined in Pineda et al. (2018). Although very similar in appearance, the left panel is not identical to Figure 4.

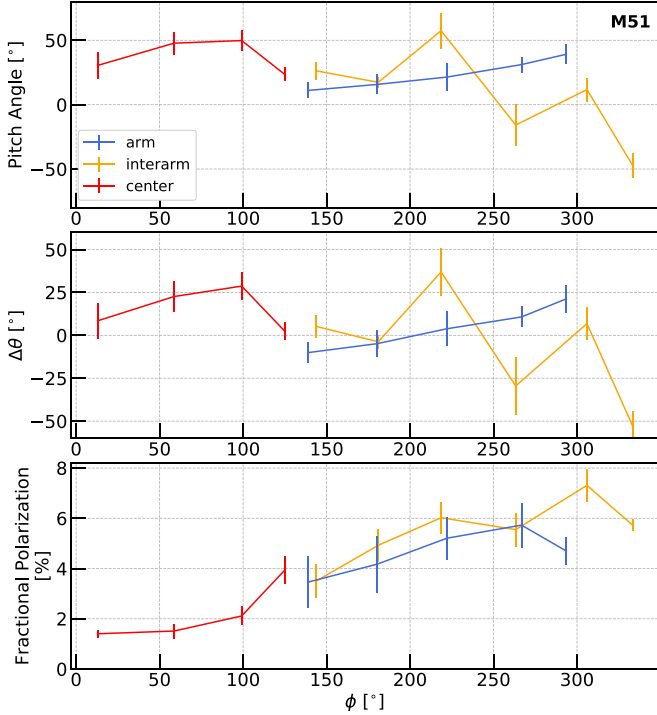


Figure 7. Pitch angle of the FIR vectors (top), the deviation of these pitch angles from the spiral arms (middle), and the fractional polarization (bottom) depending on ϕ , an angular distance along the arm defined in Figure 5, assuming Model 2 with the two pitch angles for the spiral arms. Vertical bars represent the standard deviation of the data within each bin, not an error in measurement. Red, blue, and orange represent the center, arm, and inter-arm groups, respectively.

3.3. Polarization–Intensity Relation

In our previous FIR polarimetry of galaxies (Jones et al. 2019; Lopez-Rodriguez et al. 2020), we found that the fractional polarization declines with intensity and column depth, and can often be characterized by a power-law dependency $p \propto I^\alpha$. This trend is also common in the Milky Way (e.g., Planck Collaboration et al. 2015), in particular in

molecular clouds, and is commonly plotted as $\log(p)$ versus $\log(I)$ (e.g., Jones et al. 2015; Fissel et al. 2016; Galametz et al. 2018; Chuss et al. 2019). In our previous papers, we have used fractional polarization p , but because of selection effects due to intensity cuts, the minimum measurable fractional polarization and a physical maximum in the fractional polarization are difficult to discern in that type of a plot. Instead, here we adopt plotting the polarized intensity I_p as a function of intensity or column depth. For comparison, a slope of $\alpha = -0.5$ in $\log(p)$ versus $\log(I)$ (or column depth) is equivalent to a slope of $+0.5$ in $\log(I_p)$ versus $\log(I)$. This can easily be seen through the relation $I_p = pI$.

For M51, this comparison is shown in Figure 8. The column density was computed assuming a constant temperature for the dust, and is therefore a simple multiplicative factor of the intensity. We used an emissivity modified blackbody function assuming a temperature of 25 K (Benford & Staguhn 2008). The dispersion in derived temperature found using Herschel data was only ± 1.0 K, confirming that variation in temperature across M51 will not affect our results. We define an emissivity, ϵ , which is proportional to ν^β using a dust emissivity index, β , of 1.5 from Boselli et al. (2012). We made use of the relation of the hydrogen column density, $N(\text{H} + \text{H}_2) = \epsilon / (k\mu m_{\text{H}})$, with the dust mass absorption coefficient, k , of $0.1 \text{ cm}^2 \text{ g}^{-1}$ at $250 \mu\text{m}$ (Hildebrand 1983), and the mean molecular weight per hydrogen atom, μ of 2.8 (Sadavoy et al. 2013). The maximum expected fractional polarization of 9% at $\sim 150 \mu\text{m}$ is taken from Hildebrand et al. (1995) and is within the range of dust models computed by Guillet et al. (2018) that were based on Planck observations. This upper limit nicely delineates the boundary seen in the maximum I_p measured at low column depths in M51.

Note that the lowest polarized intensities are associated with the larger $27'' \times 27''$ aperture (labeled two-beam), and averaging over this aperture could artificially reduce the computed polarization if there is significant variation in position angle of the ordered component (not the random component) to the field within the aperture. However, even a 45° variation in position angle for the ordered component

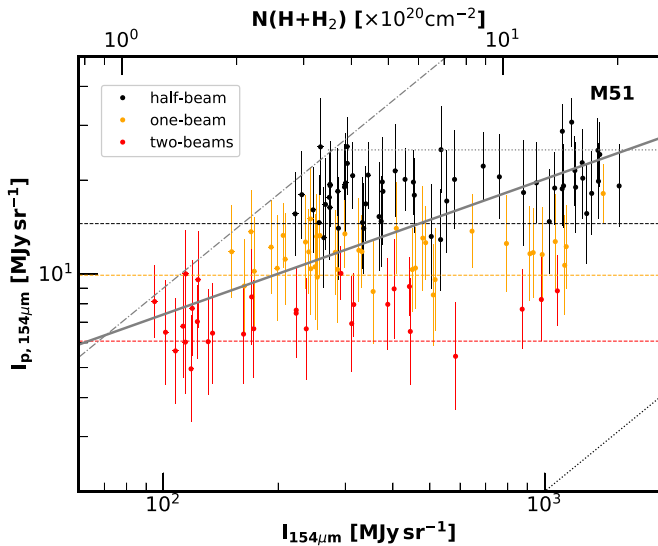


Figure 8. The debiased polarized intensity plotted against the intensity at our wavelength of $154\ \mu\text{m}$ and derived hydrogen column depth (see the text). The vector data shown in Figure 1 were used. The gray solid line is a linear fit to the data with a slope of $\log I_{p,154\ \mu\text{m}} = 0.43 \log I_{154\ \mu\text{m}}$ ($\alpha = -0.57$) calculated by an orthogonal distance regression (ODR) weighted by the squares of errors using the `scipy.odr` module. Each differently colored dashed line represents the 2.5σ observation limit estimated from the errors in Q and U in each bin size. The gray dashed-dotted line in the upper left-hand corner shows the maximum value of I_p corresponding to a maximum fractional polarization of 9% (see the text), and has a slope of $+1.0$ ($\alpha = 0$). The horizontal dotted line corresponds to an empirical upper boundary seen in the data at $I_p = 25\ \text{MJy sr}^{-1}$ and corresponds to $\alpha = -1$. Finally, the line in the lower right-hand corner shows the estimated $\pm 0.2\%$ limit in fractional polarization precision we can achieve with HAWC+ polarimetry (Jones et al. 2019) in an ideal data set.

across the aperture would only reduce the net polarization by $1/\sqrt{2}$, yet the mean for the two-beam I_p is at least a factor of three lower than for the half-beam data. Also, the large aperture results are concentrated well away from the nucleus where the spatial variation in position angle is less. The primary cause of the vertical separation between the different beam sizes in Figure 8 is S/N, rather than beam averaging. A simple linear fit (in log space) to all of the data in Figure 8 has a slope less than $+0.5$. This translates to a slope more negative than $\alpha = -0.5$ in a $\log(p)$ versus $\log(I)$ plot. Note that selection effects such as our minimum detectable polarized intensity are easy to delineate in Figure 8, as shown by the horizontal lines. Due to concerns about the effect that the minimum detectable fractional polarization has on the data points in the lower right of Figure 8, we will concentrate on examining the upper envelope of the data rather than the best-fit slope.

The upper limit in Figure 8 has a slope of $+1$ ($p = \text{constant}$) up until $N(H + H_2) \sim 3.5 \times 10^{20}\ \text{cm}^{-2}$. The slope then changes and becomes flat ($I_p = \text{constant}$), and $I_p = 25\ \text{MJy sr}^{-1}$ at greater column depth. This flat slope corresponds to a slope of $\alpha = -1$, as discussed above. For M51, the change in slope for the upper limit in polarized intensity occurs at approximately one-third the value of $N(H + H_2) \sim 10^{21}\ \text{cm}^{-2}$ found by Planck for polarization in the Milky Way (see Figure 19 in Planck Collaboration et al. 2015). As mentioned above, a strong decline in fractional polarization with column density was also found for FIR polarimetry of M82, NGC 253 (Jones et al. 2019), and NGC 1068 (Lopez-Rodriguez et al. 2020). Note that NGC 1068 has a powerful active galactic nucleus (AGN), which could create a more complex magnetic field, but most of the FIR polarimetry

samples only the much larger, surrounding disk. Lopez-Rodriguez et al. (2020) suggested three possible explanations for the decline in fractional polarization with column depth, assuming the emission is optically thin. Polarization may be reduced if there are segments along the line of sight where (1) the grains are not aligned with the magnetic field, (2) the polarization is canceled because of crossed or other variations of the magnetic field on large scales, or (3) there are sections along the line of sight that contain turbulence on much smaller scale lengths than in lower column density lines of sight, contributing total intensity, but little polarized intensity. Lopez-Rodriguez et al. (2020) considered the contribution of regions that are sufficiently dense that their higher extinction may prevent the radiation necessary for grain alignment from penetrating. These regions make a very small contribution to the FIR flux in the HAWC+ beam, simply because they are small in angular size and very cold. Although these dense cores probably experience a loss of grain alignment, they cannot have any effect on our observations of external galaxies. An additional explanation is the loss of the larger aligned grains due to radiative torque disruption (Hoang 2019) in very strong radiation fields, although any connection of this process with higher column depth is not clear.

The magnetic field in the ISM is often modeled using a combination of ordered and turbulent components (e.g., Jones et al. 1992; Miville-Deschênes et al. 2008; Planck Collaboration et al. 2016). The trend of fractional polarization with column depth (Hildebrand et al. 2009; Jones 2015; Jones et al. 2015; Fissel et al. 2016; Houde et al. 2016; Planck Collaboration et al. 2016, 2018) provides an indirect measurement of the effect of the turbulent component. For maximally aligned dust grains along a line of sight with a constant magnetic field direction, the fractional polarization in emission will be constant with optical depth τ in the optically thin regime. This case would correspond to a line in Figure 8 with a slope of $+1.0$ ($\alpha = 0$). If there is a region along the line of sight with some level of variations in the magnetic field geometry, this will result in a reduced fractional polarization. Using a simple toy model, Jones (1989) and Jones et al. (1992) showed that if the magnetic field direction varies completely randomly along the line of sight with a *single scale length* in optical depth τ (not physical length), then $p \propto \tau^{-0.5}$ (or, $I_p \propto \tau^{+0.5}$). (See Planck Collaboration et al. 2016, 2018 for a very similar model.) In real sources, more negative slopes of $\alpha = -1/2$ to -1 are found in many instances ranging from cold cloud cores to larger molecular cloud structures to whole galaxies (e.g., Fissel et al. 2016; Galametz et al. 2018; Chuss et al. 2019; Lopez-Rodriguez et al. 2020). In more recent work employing MHD simulations, King et al. (2018) and Seifried et al. (2019) found that the ordered and random components are more complicated than modeled by Jones et al. (1992). While Jones et al. (2015) argued that a slope of $\alpha = -1$ indicated complete loss of grain alignment due solely to loss of radiation that aligns grains by radiative torques (Lazarian & Hoang 2007; Andersson et al. 2015), King et al. (2019) found that including a dependency on local density for grain alignment efficiency can help explain these trends seen in large molecular clouds.

In our large (560 pc FWHM) beam, we are averaging over many molecular clouds and associated regions of massive star formation. This complicates any effort to understand the flat slope for the upper limit in Figure 8 in terms of observations and modeling for individual molecular clouds in the Milky

Way. Note that the upper limit in Figure 8 at larger column depths is dominated by the lower polarization in the central 3 kpc (diameter) region (see Figure 7). One possibility is that the field in this region has a strong component perpendicular to the plane (along our line of sight), reducing the fractional polarization. This is unlikely, given the planar field geometry seen in the central regions of edge-on spirals such as NGC 891 (this paper; Jones 1997; Montgomery & Clemens 2014), NGC 4565 (Jones 1997), and the Milky Way (e.g., Planck Collaboration et al. 2015). Starburst galaxies such as M82 (Jones 2000; Jones et al. 2019) and NGC 4631 (Krause 2009) can show a vertical field geometry in the center, but there is no indication of a massive central starburst in M51 (Pineda et al. 2018). A more likely explanation is that lines of sight through higher column density paths have segments with high turbulence on smaller scale lengths ($\ll 560$ pc) than other lower-density lines of sight. In this scenario, there are segments along the line of sight that add total intensity, but add correspondingly very little polarized intensity due to turbulence in the field on scales significantly smaller than our beam (see Figure 2 in Jones et al. 1992).

The model in Jones et al. (1992) assumes that the optical depth scale at which the magnetic field is entangled is the same throughout the entire volume. This may not always be true. First of all, the injection scale of the turbulence depends on the source of turbulent motions. The motions arising from large-scale driving forces, whether from supernovae or magnetorotational instabilities, may have a characteristic scale comparable with the scale height of the galactic disk. The local injection of turbulence arising from local instabilities or localized energy injection sources, whatever they are, can have significantly smaller scales. These significantly smaller scales form the random component that would decrease the fractional polarization compared to the simple model.

We also point out another important effect that affects the polarization. Even if the turbulence injection scale stays the same, the scale at which the magnetic field experiences significant changes in geometry may vary due to variations in the turbulence injection velocity. To understand this, one should recall the properties of MHD turbulence (e.g., Beresnyak & Lazarian 2019). If the injection velocity V_L is larger than the Alfvén velocity V_A , the turbulence is super-Alfvénic. Magnetic forces at the injection scales are too weak to affect the motion of at large scales, and at such scales the turbulence follows the usual Kolmogorov isotropic cascade with hydrodynamic motions freely moving and bending magnetic fields around. However at the scale $l_A = LM_A^{-3}$, where L is the turbulence injection scale and $M_A = V_L/V_A$, the turbulence transfers to the MHD regime with the magnetic field becoming dynamically important (Lazarian 2006). The scale l_A is the scale of the entanglement of the magnetic field. This scale determines the random walk effects on the polarization in the Jones et al. (1992) model. Evidently, l_A varies with the media magnetization and the injection velocity. These parameters change through the galaxy, and this can affect the observed fractional polarization at high column depths.³¹ To explore the nature of the turbulent component further, we next compare the radio synchrotron polarimetry with our FIR polarimetry.

³¹ In the presence of turbulent dynamo, one might expect that l_A eventually reaches L . However, the nonlinear turbulent dynamo is rather inefficient (Xu & Lazarian 2016), and therefore the temporal variations in the energy injection and in Alfvén speed are expected to induce significant variations of l_A .

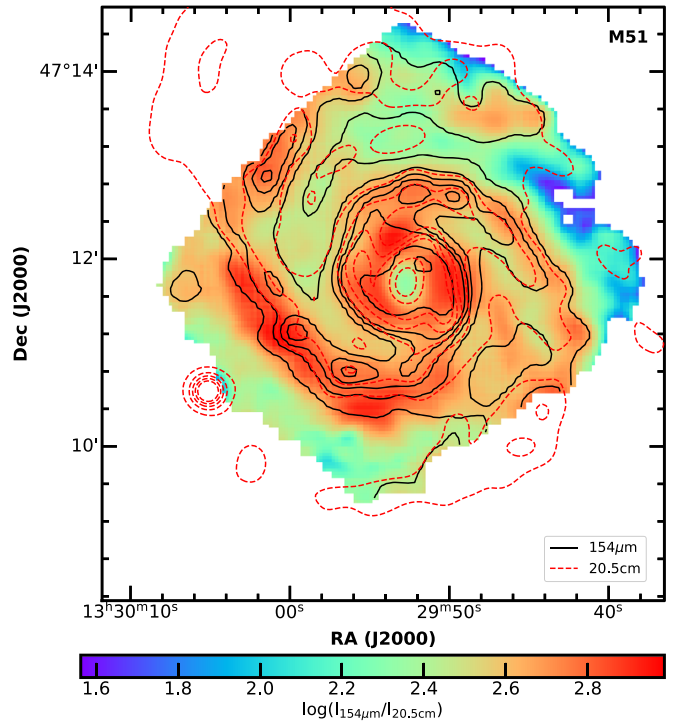


Figure 9. The ratio of the total intensity at $154 \mu\text{m}$ to that at 20.5 cm . Color represents the ratio on a logarithmic scale, $\log(I_{154 \mu\text{m}}/I_{20.5 \text{ cm}})$. The black contours indicate 100, 200, 300, 400, 500, 1000, and 1500 MJy sr^{-1} at $154 \mu\text{m}$, and the red contours indicate 0.3, 0.6, 0.9, 1.2, 1.5, 3.0, and 4.5 MJy sr^{-1} at 20.5 cm .

3.4. Radio Comparison

The magnetic field geometry of M51 seen in synchrotron polarimetry has also been extensively studied (Beck et al. 1987; Fletcher et al. 2011). We can compare the FIR emission with the synchrotron radiation at 20.5 and 6.2 cm using the data from Fletcher et al. (2011), which we obtained from ATLAS OF GALAXIES at Max Planck Institute for Radio Astronomy.³² We rotated the 6.2 cm radio vector position angles by 90° to obtain the inferred magnetic field direction and made no correction for Faraday rotation (Fletcher et al. 2011 found no statistically significant difference in fractional polarization between 3.6 and 6.2 cm wavelengths). The beam sizes at 20.5 and 6.2 cm are $15''$ and $8''$, respectively (Fletcher et al. 2011), while our beam size at $154 \mu\text{m}$ is $14''$. First, in Figure 9, we compare the total intensity at $154 \mu\text{m}$ and at 20.5 cm , which has a similar beam size to that at $154 \mu\text{m}$. We have convolved the $154 \mu\text{m}$ beam to the slightly larger beam at 20.5 cm assuming a Gaussian form for the beam shape. To be conservative in our comparison, we use only regions where all of the pixels in the $154 \mu\text{m}$ image have $I/I_{\text{err}} > 5$. In Figure 9 we show the color-coded intensity ratio on a logarithmic scale, $\log(I_{154 \mu\text{m}}/I_{20.5 \text{ cm}})$ along with the intensity contours at $154 \mu\text{m}$ and 20.5 cm .

Overall, the synchrotron emission and the FIR emission closely follow the grand design spiral pattern seen at other wavelengths. The arms are brighter than the inter-arm region at both wavelengths. However, the $154 \mu\text{m}$ emission shows greater contrast between the arm and inter-arm regions compared to the 20.5 cm emission, in many locations by up to a factor of three greater contrast. This contrast ratio is highest

³² <https://www.mpifr-bonn.mpg.de/atlasmag>

in the arm to the southeast of the center, and in the arms near (but not directly at) the center of the galaxy. Basu et al. (2012) compared Spitzer $70\ \mu\text{m}$ with 20 and 90 cm radio fluxes for four galaxies and found a greater FIR/radio flux ratio in the arms compared to the inter-arm region using 90 cm radio fluxes, but not for 20 cm fluxes. Based on our $154\ \mu\text{m}$ fluxes and the 20.5 cm data of M51, the FIR and radio measurements are not sampling volumes along the line of sight in the same way.

To first order, the dependence of synchrotron emission on cosmic-ray electron density and magnetic field strength is $I_{\text{syn}} \propto n_{\text{ce}} B^2$ (e.g., Jones et al. 1974), where I_{syn} is the synchrotron intensity, and n_{ce} is the cosmic-ray electron density. Crutcher (2012) found that the line-of-sight component (only) of the magnetic field strength (typically $2\text{--}10\ \mu\text{G}$) in the diffuse ISM of the Milky Way shows no clear trend with hydrogen density up to $n_{\text{H}} \sim 300\ \text{cm}^{-3}$, a density typical for photodissociation regions and the outer edges of molecular clouds (Hollenbach & Tielens 1999). At even higher densities, the field strength increases with density as $B \propto n_{\text{H}}^k$ with the exponent k between $2/3$ and $1/2$ (e.g., Tritsis et al. 2015; Jiang et al. 2020), but these regions occupy a small fraction of the total volume of the ISM (Hollenbach & Tielens 1999). We interpret our results as due to the synchrotron emission in M51 arising mostly in the more diffuse ISM, with denser regions contributing a smaller fraction. Assuming equipartition between the cosmic-ray energy density and the magnetic field energy density, Fletcher et al. (2011) found a moderately uniform magnetic field strength of $20\text{--}25\ \mu\text{G}$ in the arm and $15\text{--}20\ \mu\text{G}$ in the inter-arm regions of M51, suggesting that the synchrotron emission is more dependent on n_{ce} than the magnetic field strength in those regions. In the denser star-forming regions located in the spiral arms, the ratio of FIR to radio intensity must be dominated by emission from warm dust in a volume that does not contribute as much proportionally to the total synchrotron emission as it does to the FIR emission. Note that the very center of M51 has a synchrotron emission peak (Querejeta et al. 2016) due to a Seyfert 2 nucleus (Ho et al. 1997) emitting a relatively low luminosity of $L_{\text{bol}} \sim 10^{44}\ \text{erg s}^{-1}$ (Woo & Urry 2002), but the FIR emission peaks outside this region in the inner spiral arms (see Figure 5), and the AGN contributes very little to the FIR flux.

For comparison of the radio and FIR polarization, we used the observations at 6.2 cm instead of 20.5 cm because depolarization in the beam by differential Faraday rotation is less (Fletcher et al. 2011). We first convolved the 6.2 cm I , Q , and U maps to a $14''$ beam. We used the rms fluctuations in the convolved Q and U maps well off the galaxy to estimate the error in Q and U . Assuming these errors, the fractional polarization could then be computed and debiased in the same manner as our FIR polarimetry ($p_{\text{debiased}}/p_{\text{err}} > 3$), except no cut was made in the synchrotron total intensity. In Figure 10 we plot the resulting 6.2 cm radio and FIR polarization vectors overlaid on a map indicating radio intensity. The polarization vectors at both wavelengths clearly delineate the grand design spiral. There is good agreement in position angle at most locations where there is significant overlap, with one exception. At $13^{\text{h}}30^{\text{m}}02^{\text{s}} + 47^{\circ}12'30''$ the 6.2 cm vectors angle away from the arm along the bridge of emission connecting to M51b, but the FIR vectors continue to follow the spiral pattern.

The polarization position angles are compared quantitatively in Figure 11, and show a strong overall correlation between the

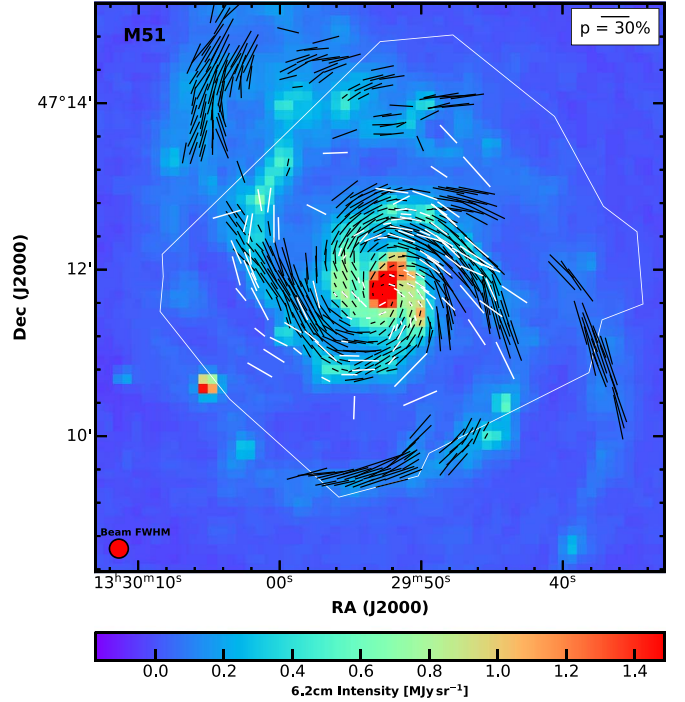


Figure 10. Fractional polarization vector maps of M51 at a wavelength of $154\ \mu\text{m}$ (white) and 6.2 cm (black). The colors show the intensity at 6.2 cm convolved to our beam at $154\ \mu\text{m}$. The scale bar for fractional polarization refers to the 6.2 cm data only. The lengths of vectors at $154\ \mu\text{m}$ are the same as those in Figure 1. The thin white line roughly outlines the observed region at $154\ \mu\text{m}$.

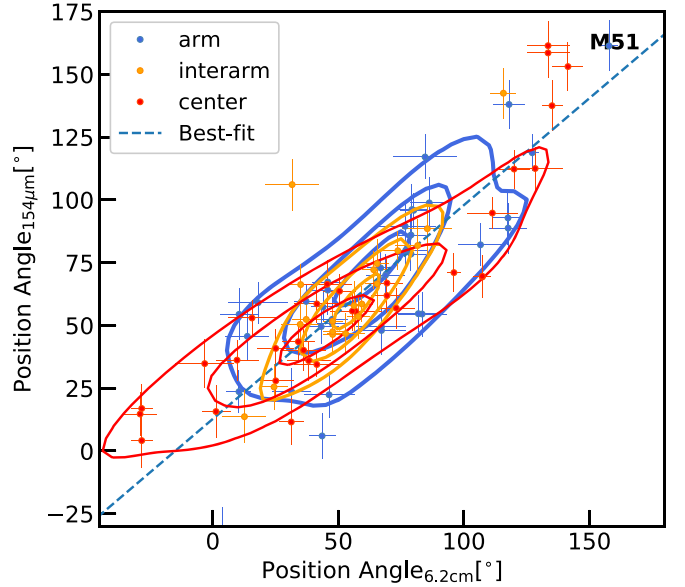


Figure 11. Plot of the $154\ \mu\text{m}$ position angle against the 6.2 cm position angle; 180° has been added to some position angles to account for the ambiguity at 0° and 180° . The Pearson correlation coefficient for each region is higher than 0.75, and the p -values are smaller than 10^{-4} . The ODR best-fit line weighted by the squares of errors to all of the data has a slope of 0.85 ± 0.12 at the $1 - \sigma$ confidence interval. The contours show the probability density of 0.3, 0.6, and 0.9 estimated by Gaussian kernel density estimation (KDE) using the `scipy.stats.Gaussian_kde` module. KDE is a way to estimate the probability density function by putting a kernel on each data point, and we used Scott's Rule to determine the width of a Gaussian kernel.

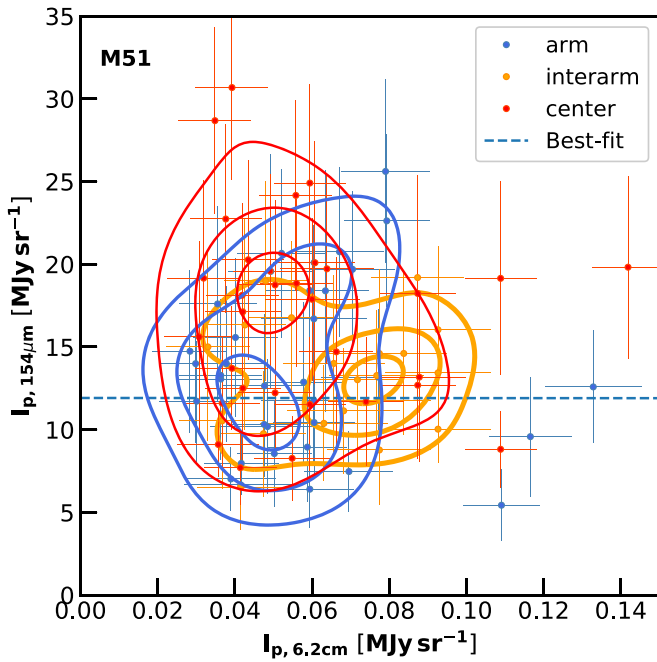


Figure 12. Plot of the polarized intensity at $154\ \mu\text{m}$ against the polarized intensity at $6.2\ \text{cm}$. The colors of the dots indicate the different regions: arm (blue), inter-arm (orange), and center (red). The symbols and contours are the same as in Figure 11. The Pearson correlation coefficients and p -values for the arm, inter-arm, and center are $[0.014, 0.94]$, $[0.1, 0.66]$, and $[0.11, 0.56]$, respectively, indicating no correlation.

radio and FIR polarization vectors. Even though the emission mechanisms are completely different, and the ISM in the respective beams is being sampled differently, we find that the inferred magnetic field geometry is essentially the same in a global sense. In other words, the FIR polarization position angle weighted by dust emission (at varying temperatures) integrated along and across the line of sight is very similar to the synchrotron position angle weighted by cosmic-ray density and field strength (squared), integrated along the *same* paths in most locations.

Our goal in this section is to investigate whether the synchrotron observations can shed light on the underlying cause of the strong decline in fractional polarization with intensity found at FIR wavelengths. For example, consider the hypothesis that there are segments across the beam and along a line of sight associated with dense gas and dust that have field geometries highly disordered in our beam relative to the larger-scale field, adding significant FIR total intensity but very little polarized intensity. In lower column depth lines of sight, these segments (perhaps giant molecular clouds) may be absent or relatively rare, making proportionally less of a contribution to the total FIR intensity, and they have less effect on the fractional polarization. Since the synchrotron polarimetry is sampling the same line of sight differently, these segments may contribute differently to the polarized synchrotron emission.

We compare the polarized intensity between the FIR and the radio in Figure 12 and the fractional polarization in Figure 13. Although this may seem redundant, there are important differences between the polarized intensity and the fractional polarization. In the diffuse ISM there is no clear dependence of dust grain alignment on magnetic field strength (Jones 1989, 2015; Planck Collaboration et al. 2015). Thus, in the FIR, neither polarized intensity nor fractional

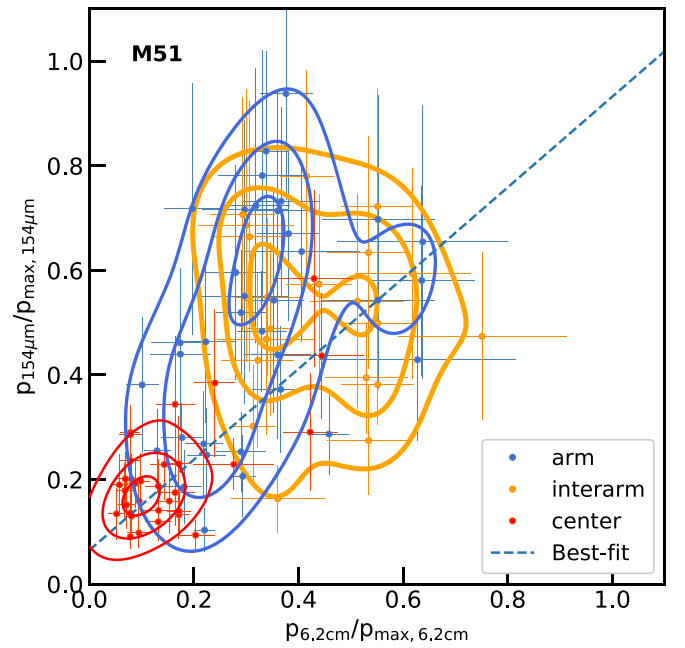


Figure 13. Plot of the normalized fractional polarization at $154\ \mu\text{m}$ against the normalized fractional polarization at $6.2\ \text{cm}$. The normalization factor was 9% at $154\ \mu\text{m}$ and 70% at $6.2\ \text{cm}$ (see the text). The symbols and contours are the same as in Figure 11. The Pearson correlation coefficients and p -values for the arm, inter-arm, and center are $[0.38, 0.02]$, $[-0.06, 0.82]$, and $[0.68, 10^{-5}]$, respectively. The correlation coefficient for the entire data set is 0.61 with a p -value of 10^{-9} . The slope of the best-fit line to all data is 0.87 ± 0.22 .

polarization are dependent on magnetic field strength, but they are strongly dependent on the magnetic field geometry (Jones et al. 1992; Planck Collaboration et al. 2016, 2018). For synchrotron emission, the polarized intensity is dependent on magnetic field strength and the magnetic field geometry, but the fractional polarization is dependent only on the field geometry, as is the case in the FIR. Thus, we should expect no correlation between the polarized intensity at the two wavelengths, but there should be a correlation between their fractional polarization if they are indeed sampling the same net magnetic field geometry.

In Figure 12, there is no correlation seen between the polarized intensity at FIR and $6.2\ \text{cm}$ wavelengths for the higher surface brightness central region (red contours), the arm region (blue contours), or the inter-arm region (orange contours). For fractional polarization (Figure 13), we have normalized both the FIR and $6.2\ \text{cm}$ polarization with respect to their maximum expected values. We used $p_{\text{max}} = 70\%$ at $6.2\ \text{cm}$ based on computational results in Jones & Odell (1977). There is a modest correlation for the entire data set, with the greatest correlation in the central region. Note again that the central region has very weak fractional polarization at both wavelengths.

For the arms (see Figure 7), we do not see a significant difference in fractional polarization for our FIR observations when compared to the inter-arm region. At radio wavelengths, Fletcher et al. (2011) found that the inter-arm region has a greater fractional polarization than the arms (see their Table 2), which they attribute to a more ordered field in the inter-arm region. This difference between FIR and radio observations suggests that variations in the magnetic field geometry are similar between the arm and inter-arm regions as sampled by FIR polarimetry, but that the greater column depth in the arms

may have caused enough Faraday depolarization across the beam to further reduce the fractional polarization at 6.2 cm. Finally, the high surface brightness central region shows very weak fractional polarization at both wavelengths. Here the radio and FIR beams must sample a more complex magnetic field geometry with highly turbulent segments across the beam and along individual lines of sight within the beam. This more complex magnetic field geometry reduces the net fractional polarization at both FIR and radio wavelengths with, perhaps, added Faraday depolarization in the beam at 6.2 cm. Polarized emission in this region is sampled differently at the two wavelength regimes, hence producing uncorrelated polarized intensities. Yet the net position angles strongly agree, the fractional polarizations are moderately correlated, and both techniques yield the same net magnetic field geometry in the beam. We will explore this interpretation more carefully in a later paper.

4. NGC 891

4.1. Introduction

At a distance of 8.4 Mpc (Tonry et al. 2001), NGC 891 presents an interesting case for an edge-on galaxy that is a late-type spiral with a similar mass and size as the Milky Way (Karachentsev et al. 2004). Like the Milky Way, NIR polarimetry of NGC 891 reveals a general pattern of a magnetic field lying mostly in the plane (Jones 1997; Montgomery & Clemens 2014). Radio synchrotron observations are also consistent with this general field geometry, but extend well out of the disk into the halo (Sukumar & Allen 1991; Krause 2009). According to models by Wood & Jones (1997), highly polarized scattered light may be a contaminant affecting the optical and NIR polarization in edge-on systems producing polarization null points at locations along the disk, well away from the nucleus. Montgomery & Clemens (2014) did not find evidence for the predicted null points along the disk, but did find null points at other locations that they associate with an embedded spiral arm along the line of sight. Optical polarimetry (Scarrott & Draper 1996) revealed (unexpected) polarization mostly vertical to the plane, with only a few locations in the northeast showing polarization parallel to the disk. The optical polarimetry was attributed to vertical magnetic fields, but Montgomery & Clemens (2014) argued that the optical polarimetry was contaminated by scattered light. Scattering in the halo of light from stars in the disk and the bulge, as modeled by Wood & Jones (1997) and Seon (2018), may be a more likely explanation for the optical polarization. Note that the NIR and FIR polarimetry penetrate much deeper into the disk than is possible at optical wavelengths.

4.2. The Planar Field Geometry

Our 154 μm polarimetry of NGC 891 is shown in Figure 14 where the colors and symbols are the same as described for M51. To show the magnetic field geometry more clearly, we set the fractional polarization to a constant value in Figure 15. Along the center of the edge-on disk, the vectors align very close to the plane of the disk everywhere except in the extreme northeast. There, a few vectors are perpendicular to the disk, suggesting a vertical magnetic field, which will be discussed below. Clearly evident in both the NIR polarimetry (Jones 1997; Montgomery & Clemens 2014) and the radio

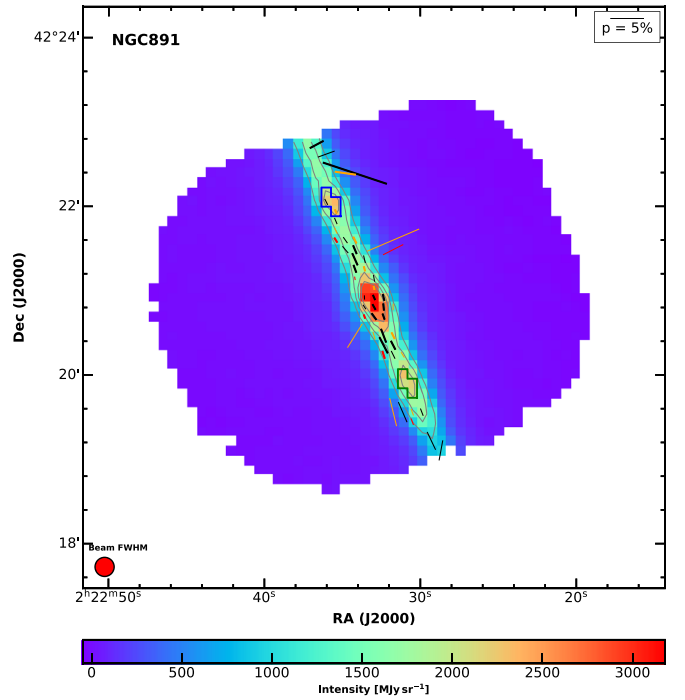


Figure 14. Polarization vector map of NGC 891 at a wavelength of 154 μm , in which the E vectors are rotated 90° to represent the inferred magnetic field direction. Data points using a square $6''.8 \times 6''.8$ “half” beam are plotted in black. Data points using a $13''.6 \times 13''.6$ “full” beam are plotted in orange, and red vectors are computed using a $27''.2 \times 27''.2$ square beam. The red disk in the lower left-hand corner indicates the FWHM footprint of the HAWC+ beam on the sky at 154 μm . Vectors with $S/N \geq 3:1$ have thick lines, and vectors with S/N from 2.5:1 to 3:1 have thin lines. The color map represents the 154 μm continuum intensity, and gray contours show 1000, 1500, 2000, and 2500 MJy sr^{-1} . The two regions discussed in the text are outlined by blue and green boxes.

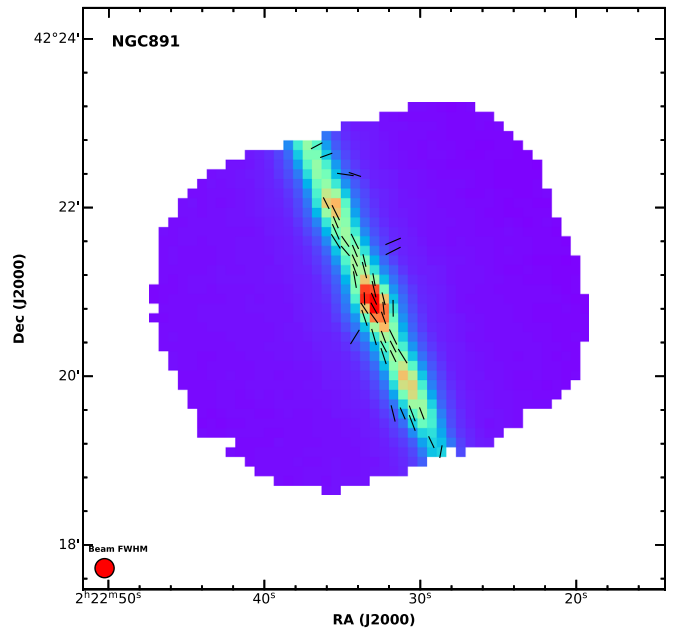


Figure 15. Same as Figure 14, except that all of the polarization vectors have been set to the same length to better illustrate the position angles.

synchrotron polarimetry (Sukumar & Allen 1991; Krause 2009) is an $\sim 15^\circ$ tilt for many of the polarization vectors relative to the galactic plane to the northeast of the nucleus. Figure 8 in

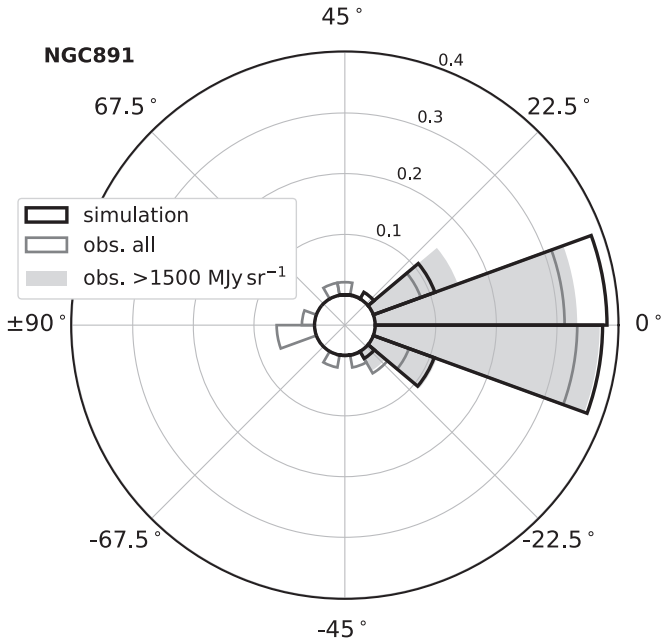


Figure 16. Distribution of $\Delta\theta$ between the position angle of our polarization vectors and the major axis of the galaxy. A positive value means counterclockwise rotation from the major axis. The gray solid line shows the distribution of all data, and the gray shaded region shows that of the data only in the region with intensity higher than 1500 MJy sr^{-1} . The black solid line indicates a simulation made under the assumption that the polarization vectors follow the major axis of the galaxy, and only errors in the data contribute to the dispersion.

Montgomery & Clemens (2014) best illustrates this offset, and it is not seen in the FIR vectors.

The distribution of $\Delta\theta$ between the position angle of our rotated polarization vectors and the major axis is shown in Figure 16. We used 21° as the position angle for the major axis of the galaxy (Sofue et al. 1987). In an identical manner to M51, we simulated the expected distribution under the assumption that the polarization vectors intrinsically follow the major axis of the galaxy, and only observation error causes any deviation. In Figure 16 the gray solid line shows the distribution for all data whereas the solid, light-gray bars show the distribution only for regions with intensity higher than 1500 MJy sr^{-1} , which isolates the bright dust lane (see Figure 14). When constrained to the bright dust lane, the simulated distribution and the observed distribution are very similar, with a formal p -value for this comparison is 0.97.

Although more penetrating than optical polarimetry, NIR polarimetry at $1.65 \mu\text{m}$ still experiences significant interstellar extinction in dusty, edge-on systems (e.g., Jones 1989; Clemens et al. 2012). In a beam containing numerous individual stars mixed in with dust, the NIR fractional polarization in extinction will saturate at $A_V \sim 13$, or $A_H \sim 2.5$ (Figure 4 in Jones 1997). At $154 \mu\text{m}$, the disk is essentially optically thin ($\tau \sim 0.05$ for $A_V = 100$; Jones et al. 2015); thus, the FIR polarimetry penetrates through the entire edge-on disk. One interpretation of our FIR polarimetry is that the NIR is sampling the magnetic field geometry on the near side of the disk, where the net field geometry shows a tilt in many locations, perhaps due to a warp in the disk (Oosterloo et al. 2007). The FIR polarimetry is sampling the magnetic field geometry much deeper into the disk, where the net field geometry is very close to the plane. The radio synchrotron polarimetry at 3.6 cm from Krause (2009) used a much larger

beam of $84''$, and could be influenced by strong Faraday depolarization in the small portion of their beam that contains the disk, which has a much greater column depth than the face-on M51. Their net position angles may be sensitive only to the field geometry in the rest of the beam, also possibly influenced by the warp. Whatever the explanation, the FIR polarimetry along the disk within $2'$ of the nucleus clearly indicates that the magnetic field direction deep inside NGC 891 lies very close to the galactic plane.

There are two regions of enhanced intensity in the disk about $1'$ on either side of the nucleus, designated by colored outlines in Figure 14. These locations also correspond to intensity enhancements seen in a radio map of the galaxy made by combining Low-Frequency Array (LOFAR) and VLA observations (Mulcahy et al. 2018), and in PACS $70 \mu\text{m}$ observations as well (Bocchio et al. 2016). Those studies attribute such enhancements to the presence of spiral arms and the enhanced star formation associated with them, but do not present a model of the emission from the disk. These features are $3\text{--}4 \text{ kpc}$ from the center, not untypical for spiral arms. For example, rotate M51 about a north–south axis to create an edge-on spiral, and there would be enhancements in FIR emission on either side from the center at this distance. The polarization is very low in the southern region, at the limits of our detection. The polarization is also quite low in the northern bright spot. As with M51 and discussed below for NGC 891, the fractional polarization is anticorrelated with intensity, so this may not be unexpected, but the polarization in the southern spot in particular is exceptionally low. Montgomery & Clemens (2014) also found regions along the disk where the NIR polarimetry was very low. They suggested the observer was looking down along a spiral arm, where the magnetic field is largely *along* (parallel to) the line of sight, which results in much lower polarization (e.g., Jones & Whittet 2015). This could be the explanation for the very low polarization in our two bright spots, and could also explain the origin of the enhancement in intensity, since a line of sight down a spiral arm will pass through more star-forming regions. However, the regions of low polarization seen at NIR wavelengths and FIR wavelengths are not coincident; rather, the NIR null points are located farther out from the center of the galaxy. Given the greater penetrating power of FIR observations, it is possible that we are viewing more deeply embedded spiral features than are accessible by NIR polarimetry, which is more sensitive to the front side of the disk.

4.3. Vertical Fields

Dust in emission is detected above and below the disk of NGC 891. At FIR wavelengths, Bocchio et al. (2016) found a thick disk component to the dust emission with a scale height of $\sim 1.5 \text{ kpc}$ ($36''$). At NIR wavelengths, Aoki et al. (1991) measured a scale height of 350 pc ($8''.6$) for the stellar component, significantly smaller than the dust scale height. There are a handful of vectors in Figure 14 that lie off the bright disk in the halo of NGC 891. Five of these vectors are consistent with a vertical magnetic field geometry, in strong contrast to the disk. At optical wavelengths, Howk & Savage (1997) imaged vertical fingers of dust that stretch up to 1.5 kpc off the plane, also suggestive of a vertical field extending into the halo. Optical polarimetry of the northeast portion of the disk (Scarrott & Draper 1996) has a few vectors parallel to the plane, but the majority are perpendicular to the plane. Although

the optical polarimetry was interpreted as evidence for vertical magnetic fields by Scarrott & Draper (1996), the NIR polarimetry from Montgomery & Clemens (2014) and modeling by Wood & Jones (1997) and Seon (2018) indicate that scattering of light originating from the central region can have a major effect. Without significant dust to shine through (causing interstellar extinction), it is difficult to produce measurable interstellar polarization in *extinction* (Jones & Whittet 2015).

The optical polarization vectors in Scarrott & Draper (1996) are typically 1%–2% in magnitude $\sim 20''$ off the plane using a $12''$ beam. Based on our $154\ \mu\text{m}$ contours, this corresponds to about $400\ \text{MJy sr}^{-1}$, or $A_V \sim 0.4$. The historically used empirical maximum for interstellar polarization in extinction at V is $p(\%) = 3A_V$ (Serkowski et al. 1975), but recent work shows this can be as high as $p(\%) = 5A_V$ for low-density lines of sight out of the Galactic plane (Panopoulou et al. 2019). For an optimum geometry of a screen of dust with a uniform magnetic field geometry entirely in front of the stars in the halo, a maximum fractional polarization of $\sim 2\%$ would be expected. For a mix of dust and stars along the line of sight and turbulence in the magnetic field, the expected fractional polarization would be even less. Although Howk & Savage (1997) estimated $A_V \sim 1$ within some of the vertical filaments, which are only $2''$ – $3''$ wide, considerable unpolarized starlight emerging between the filaments would be contributing as well. At optical wavelengths it is not clear that there is enough extraplanar dust to shine through to cause significant polarization in extinction $\sim 20''$ off the disk, but plenty of dust to scatter light (a mean $\tau_{\text{sc}} \sim 0.3$ at V) from stars in the disk and bulge. As with M51, the striking similarity between the optical polarimetry vectors and our FIR vectors cannot be denied, and remains a mystery when the non-detection at NIR wavelengths is considered.

Polarimetry at FIR wavelengths is measuring the *emission* from warm dust, and generally the fractional polarization is observed to be highest at low FIR optical depths (Planck Collaboration et al. 2015; Fissel et al. 2016; Chuss et al. 2019), but there must be enough warm dust in the beam to produce a measurable signal. For our observations of NGC 891, a vertical scale height of 1.5 kpc corresponds to $36''$, or 2.7 beamwidths for our $154\ \mu\text{m}$ observations. The surface brightness at this vertical distance for most of the disk is $\sim 100\ \text{MJy sr}^{-1}$ ($A_V \sim 0.1$), which is near the limit of our detectability of statistically significant fractional polarization. At 1.5 beams ($20''$) off the plane, the surface brightness ranges from 300 to $500\ \text{MJy sr}^{-1}$, a range in which 5% polarization is easily detectable. Note that, if NGC 891 were face-on, this halo dust emission would contribute very little to the total flux in our beam compared to the disk.

We draw the tentative conclusion that the several $154\ \mu\text{m}$ vectors in the halo that are perpendicular to the disk are indicative of a vertical magnetic field geometry in the halo of NGC 891. No evidence for vertical fields was found in radio observations by Krause (2009), but they had a very large $84''$ beam. Using a $20''$ beam, Sukumar & Allen (1991) found hints of a vertical field on the eastern side of the southwestern extension of the disk, just east of the region outlined in green in Figure 14, where we suggest we are looking down a spiral arm. Mora-Partiarroyo et al. (2019) made radio observations of NGC 4631, an edge-on galaxy with an even more extended halo than NGC 891, using a $7''$ beam. They found that the magnetic field in the halo is characterized by strong vertical components.

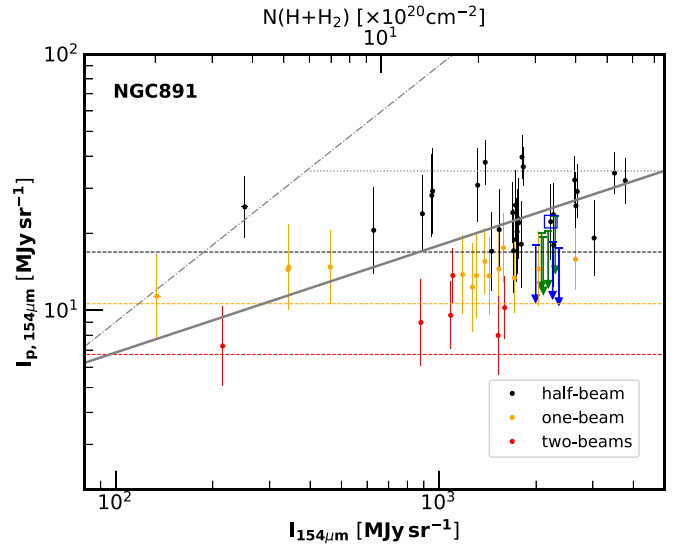


Figure 17. Plot of the polarized intensity against the intensity at $154\ \mu\text{m}$. The vectors shown in Figure 14 were used. A gray solid line is a fit to the data, where $\log I_{p, 154\ \mu\text{m}} = 0.42 \log I_{154\ \mu\text{m}}$. All other lines are the same as in Figure 8. The green and blue upper limits and boxed blue points are described in Section 4.4.

Examination of the Faraday depth pattern in the halo of NGC 4631 indicated large-scale field reversals in part of the halo, suggesting giant magnetic ropes, oriented perpendicular to the disk, but with alternating field directions. Our FIR polarimetry, which is not affected by Faraday rotation, cannot distinguish field reversals (since the grain alignment is the same), and would reveal only the coherent, vertical geometry, such as we see in our observations in the halo of NGC 891. Brandenburg & Furuya (2020) presented numerical results of mean-field dynamo model calculations for NGC 891 as a representative case for edge-on disk systems, but our observations do not have enough vectors for a detailed comparison.

4.4. Polarization–Intensity Relation

Figure 17 plots the polarized intensity against the intensity and column depth for NGC 891. Other than using a temperature of 24 K for the dust (Hughes et al. 2014), the procedure for calculating the column depth from the surface brightness at $154\ \mu\text{m}$ is the same as for M51. NGC 891 shows a clear trend in I_p versus I , with a similar slope to that found for M51, and shows evidence for a horizontal upper limit as well. However, unlike M51, the decrease in polarization in the bulge is not quite as strong, and more of the very low fractional polarization values are located in the disk away from the nucleus. Also unlike M51, the data at lower column depths in either the disk or the halo generally lie well below the upper limit of $p = 9\%$ in Figure 17, although this may be partially due to a smaller number of vectors compared to M51. Presumably, the more complex line-of-sight magnetic field geometry through an edge-on galaxy reduces the net polarization compared to the face-on geometry for M51. Spiral structure seen edge-on can present a range of projected magnetic field directions along a line of sight, crossing nearly perpendicular to some arms, but more down along other arms in our beam.

The two regions with low polarization delineated in Figure 14 by green and blue outlines are shown in Figure 17 using the same colors. These are the two regions we speculated

were lines of sight down a spiral arm, reducing the fractional polarization. There is only one detection in these regions, and the rest of the data points are 3σ upper limits, indicating a low fractional polarization compared to the general trend. Until a model of the spiral structure in NGC 891 is developed, we can only identify these two locations as potential indicators of spiral features.

5. Conclusions

In this work we report $154\ \mu\text{m}$ polarimetry of the face-on galaxy M51 and the edge-on galaxy NGC 891 using HAWC+ on SOFIA with projected beam sizes of 560 and 550 pc, respectively. We have drawn the following conclusions:

1. For M51, the FIR polarization vectors (rotated 90° to infer the magnetic field direction) generally follow the spiral pattern seen in other tracers. The dispersion in position angle with respect to the spiral features is greater than can be explained by observational errors alone. For the arm region, the position angles may be consistent with the spiral pattern, but uncertainties in the contribution of a random component to the magnetic field prevent us from making a more definitive statement. The central region, however, clearly shows a more open spiral pattern than that seen in the CO and dust emission.
2. Even though the FIR (warm dust) and 6.2 cm (synchrotron) emission mechanisms involve completely different physics and sample the line of sight differently, their polarization position angles are well correlated. The ordered field in M51 must connect regions dominating the synchrotron polarization and the FIR polarization in a simple way.
3. Both the 6.2 cm synchrotron and FIR emission show very low fractional polarization in the high surface brightness central region in M51. There is a moderate correlation in fractional polarization between the two wavelengths, yet the polarized intensity shows no correlation anywhere in the galaxy. The low polarization is likely caused by an increase in the complexity of the magnetic field and a greater contribution from more turbulent segments in the beam and down lines of sight within the beam. The lack of correlation between polarized intensity at both wavelengths indicates that the magnetic field strength, which influences the polarized intensity at 6.2 cm, but not in the FIR, is not the cause of the low fractional polarization at FIR wavelengths. Lack of grain alignment can also be ruled out. We conclude that along individual lines of sight, different segments must be contributing to the total and polarized intensity in different proportions at the two wavelengths.
4. Within the arms themselves, we find a similar fractional polarization to the inter-arm region in dust emission, unlike the synchrotron emission, which has a lower fractional polarization in the arms relative to the inter-arm region. This suggests that the turbulent component to the magnetic field (as sampled by FIR emission) is similar to that in the inter-arm region, but that the synchrotron emission may be additionally influenced by some Faraday depolarization in the arms.
5. For NGC 891, the FIR vectors within the high surface brightness contours of the edge-on disk are tightly constrained to the plane of the disk. Dispersion in

position angle about the plane can be explained by errors in the measurements alone. This result is in contrast to radio and NIR polarimetry, which show a clear departure from planar at many locations along the disk. We are probably probing deeper into the disk of NGC 891 than is possible with NIR and synchrotron polarimetry, revealing a very planar magnetic field geometry in the interior of the galaxy.

6. There are two locations along the disk of NGC 891 that show very low polarization and may be locations where the line of sight is along a major spiral arm, resulting in lower fractional polarization. These two locations line up with FIR intensity contours, but do not correspond to nulls in the NIR polarimetry, thought to be due to the same cause. Likely, the NIR is sensitive to spiral features that are closer to the front side of the disk due to extinction obscuring such features deeper into the disk.
7. There is tentative evidence for the presence of vertical fields in the FIR polarimetry of NGC 891 in the halo that is not present at NIR wavelengths and is only hinted at in radio observations. At FIR wavelengths there is dust above and below the disk in emission, but this dust may not be enough to produce polarization in extinction at optical or NIR wavelengths.

These data are the first HAWC+ observations of M51 and NGC 891 in polarimetry mode. The brighter regions within the spiral arms of M51 and the disk of NGC 891 are well measured. However, the inter-arm regions in M51 and the halo of NGC 891 are less well measured, and these two regions will require deeper observations to better quantify the arm–inter-arm comparison in M51 and the presence of vertical fields in NGC 891.

We thank Larry Rudnick for many useful discussions on radio polarimetry.










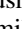



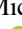
Portions of this work were carried out at the Jet Propulsion Laboratory, operated by the California Institute of Technology under a contract with NASA.




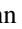




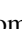


The authors wish to thank Northwestern’s Center for Interdisciplinary Exploration and Research in Astrophysics (CIERA) for providing technical support during the development and usage of the HAWC+ data analysis pipeline.

A.L. acknowledges support from National Science Foundation grant AST 1715754.

Facility: SOFIA(HAWC+).

ORCID iDs

Terry Jay Jones  <https://orcid.org/0000-0002-8716-6980>
 Jin-Ah Kim  <https://orcid.org/0000-0001-8380-9988>
 Mark R. Morris  <https://orcid.org/0000-0002-6753-2066>
 Jorge L. Pineda  <https://orcid.org/0000-0001-8898-2800>
 Dominic J. Benford  <https://orcid.org/0000-0002-9884-4206>
 David T. Chuss  <https://orcid.org/0000-0003-0016-0533>
 Daniel A. Dale  <https://orcid.org/0000-0002-5782-9093>
 L. M. Fissel  <https://orcid.org/0000-0002-4666-609X>
 Paul F. Goldsmith  <https://orcid.org/0000-0002-6622-8396>
 Ryan T. Hamilton  <https://orcid.org/0000-0001-6350-2209>
 Shaul Hanany  <https://orcid.org/0000-0002-8702-6291>
 Leslie W. Looney  <https://orcid.org/0000-0002-4540-6587>
 Joseph M. Michail  <https://orcid.org/0000-0003-3503-3446>
 Giles Novak  <https://orcid.org/0000-0003-1288-2656>

Fabio P. Santos  <https://orcid.org/0000-0002-9650-3619>
 Kartik Sheth  <https://orcid.org/0000-0002-5496-4118>
 Javad Siah  <https://orcid.org/0000-0001-5389-5635>
 Johannes Staguhn  <https://orcid.org/0000-0002-8437-0433>
 Ian W. Stephens  <https://orcid.org/0000-0003-3017-4418>
 Konstantinos Tassis  <https://orcid.org/0000-0002-8831-2038>
 John E. Vaillancourt  <https://orcid.org/0000-0001-8916-1828>
 Derek Ward-Thompson  <https://orcid.org/0000-0003-1140-2761>
 Michael Werner  <https://orcid.org/0000-0003-4990-189X>
 Edward J. Wollack  <https://orcid.org/0000-0002-7567-4451>
 Ellen G. Zweibel  <https://orcid.org/0000-0003-4821-713X>

References

- Andersson, B.-G., Lazarian, A., & Vaillancourt, J. E. 2015, *ARA&A*, **53**, 501
 Aoki, T. E., Hiromoto, N., Takami, H., et al. 1991, *PASJ*, **43**, 755
 Basu, A., Roy, S., & Mitra, D. 2012, *ApJ*, **756**, 141
 Beck, R. 2015, *A&ARv*, **24**, 4
 Beck, R., & Gaensler, B. M. 2004, *NewAR*, **48**, 1289
 Beck, R., Klein, U., & Wielebinski, R. 1987, *A&A*, **186**, 95
 Beck, R., & Wielebinski, R. 2013, *Planets, Stars and Stellar Systems*. Volume 5: Galactic Structure and Stellar Populations (Dordrecht: Springer), 641
 Benford, D. J., & Staguhn, J. G. 2008, in *ASP Conf. Ser.* 381, *The Second Annual Spitzer Science Center Conference: Infrared Diagnostics of Galaxy Evolution*, ed. R.-R. Chary, H. I. Teplitz, & K. Sheth (San Francisco, CA: ASP), 132
 Beresnyak, A., & Lazarian, A. 2019, *Turbulence in Magnetohydrodynamics* (Berlin: De Gruyter)
 Bocchio, M., Bianchi, S., Hunt, L. K., et al. 2016, *A&A*, **586**, A8
 Boselli, A., Ciesla, L., Cortese, L., et al. 2012, *A&A*, **540**, A54
 Brandenburg, A., & Furuya, R. S. 2020, arXiv:2003.07284
 Chuss, D. T., Andersson, B.-G., Bally, J., et al. 2019, *ApJ*, **872**, 187
 Clemens, D. P., Pinnick, A. F., Pavel, M. D., et al. 2012, *ApJS*, **200**, 19
 Crutcher, R. M. 2012, *ARA&A*, **50**, 29
 Davis, B. L., Berrier, J. C., Shields, D. W., et al. 2012, *ApJS*, **199**, 33
 Fissel, L. M., Ade, P. A. R., Angilè, F. E., et al. 2016, *ApJ*, **824**, 134
 Fletcher, A. 2010, in *ASP Conf. Ser.* 438, *The Dynamic Interstellar Medium: A Celebration of the Canadian Galactic Plane Survey*, ed. R. Kothés, T. L. Landecker, & A. G. Willis (San Francisco, CA: ASP), 197
 Fletcher, A., Beck, R., Shukurov, A., Berkhuijsen, E. M., & Horellou, C. 2011, *MNRAS*, **412**, 2396
 Galametz, M., Maury, A., Girat, J. M., et al. 2018, *A&A*, **616**, A139
 Goldreich, P., & Kylafis, N. D. 1981, *ApJL*, **243**, L75
 Guillet, V., Fanciullo, L., Verstraete, L., et al. 2018, *A&A*, **610**, A16
 Harper, D. A., Runyan, M. C., Dowell, C. D., et al. 2018, *JAI*, **7**, 1840008
 Hildebrand, R. H. 1983, *QJRS*, **24**, 267
 Hildebrand, R. H., Dotson, J. L., Dowell, C. D., et al. 1995, in *ASP Conf. Ser.* 73, *Airborne Astronomy Symp. on the Galactic Ecosystem: From Gas to Stars to Dust* (San Francisco, CA: ASP), 97
 Hildebrand, R. H., Kirby, L., Dotson, J. L., et al. 2009, *ApJ*, **696**, 567
 Ho, L. C., Filippenko, A. V., & Sargent, W. L. W. 1997, *ApJS*, **112**, 315
 Hoang, T. 2019, *ApJ*, **876**, 13
 Hollenbach, D. J., & Tielens, A. G. G. M. 1999, *RvMP*, **71**, 173
 Houde, M., Fletcher, A., Beck, R., et al. 2013, *ApJ*, **766**, 49
 Houde, M., Hull, C. L. H., Plambeck, R. L., Vaillancourt, J. E., & Hildebrand, R. H. 2016, *ApJ*, **820**, 38
 Howard, S., & Byrd, G. G. 1990, *AJ*, **99**, 1798
 Howk, J. C., & Savage, B. D. 1997, *AJ*, **114**, 2463
 Hu, T., Shao, Z., & Peng, Q. 2013, *ApJL*, **762**, L27
 Hughes, T. M., Baes, M., Fritz, J., et al. 2014, *A&A*, **565**, A4
 Jiang, H., Li, H.-b., & Fan, X. 2020, *ApJ*, **890**, 153
 Jones, A., Wang, L., Krisciunas, K., et al. 2012, *ApJ*, **748**, 17
 Jones, T. J. 1989, *ApJ*, **346**, 728
 Jones, T. J. 1997, *AJ*, **114**, 1393
 Jones, T. J. 2000, *AJ*, **120**, 2920
 Jones, T. J. 2015, *Astrophysics and Space Science Library*, Vol. 407, *Magnetic Fields in Diffuse Media* (Berlin: Springer), 153
 Jones, T. J., Bagley, M., Krejny, M., et al. 2015, *AJ*, **149**, 31
 Jones, T. J., Dowell, C. D., Lopez Rodriguez, E., et al. 2019, *ApJL*, **870**, L9
 Jones, T. J., Klebe, D., & Dickey, J. M. 1992, *ApJ*, **389**, 602
 Jones, T. J., & Whittet, D. C. B. 2015, in *Polarimetry of Stars and Planetary Systems*, ed. L. Kolokolova, J. Hough, & A. Levasseur-Regourd (Cambridge: Cambridge Univ. Press), 147
 Jones, T. W., & Odell, S. L. 1977, *ApJ*, **214**, 522
 Jones, T. W., O'dell, S. L., & Stein, W. A. 1974, *ApJ*, **188**, 353
 Karachentsev, I. D., Karachentseva, V. E., Huchtmeier, W. K., et al. 2004, *AJ*, **127**, 2031
 King, P. K., Chen, C.-Y., Fissel, L. M., et al. 2019, *MNRAS*, **490**, 2760
 King, P. K., Fissel, L. M., Chen, C.-Y., et al. 2018, *MNRAS*, **474**, 5122
 Kobulnicky, H. A., Molnar, L. A., & Jones, T. J. 1994, *AJ*, **107**, 1433
 Koda, J., Scoville, N., Sawada, T., et al. 2009, *ApJL*, **700**, L132
 Kraus, J. D. 1966, *Radio Astronomy* (New York: McGraw-Hill)
 Krause, M. 2009, *RMxAC*, **36**, 25
 Kronberg, P. P. 1994, *RPPh*, **57**, 325
 Lazarian, A. 2006, *ApJL*, **645**, L25
 Lazarian, A., Esquivel, A., & Crutcher, R. 2012, *ApJ*, **757**, 154
 Lazarian, A., & Hoang, T. 2007, *MNRAS*, **378**, 910
 Li, H.-B., & Henning, T. 2011, *Natur*, **479**, 499
 Lopez-Rodriguez, E., Dowell, C. D., Jones, T. J., et al. 2020, *ApJ*, **888**, 66
 Mao, S. A., Zweibel, E., Fletcher, A., et al. 2015, *ApJ*, **800**, 92
 McQuinn, K. B. W., Skillman, E. D., Dolphin, A. E., et al. 2016, *ApJ*, **826**, 21
 Miville-Deschênes, M.-A., Ysard, N., Lavabre, A., et al. 2008, *A&A*, **490**, 1093
 Montgomery, J. D., & Clemens, D. P. 2014, *ApJ*, **786**, 41
 Mora-Partiarroyo, S. C., Krause, M., Basu, A., et al. 2019, *A&A*, **632**, A11
 Mulcahy, D. D., Horneffer, A., Beck, R., et al. 2018, *A&A*, **615**, A98
 Oosterloo, T., Fraternali, F., & Sancisi, R. 2007, *AJ*, **134**, 1019
 Panopoulou, G. V., Hensley, B. S., Skolidis, R., et al. 2019, *A&A*, **624**, L8
 Patrikeev, I., Fletcher, A., Stepanov, R., et al. 2006, *A&A*, **458**, 441
 Pavel, M. D., & Clemens, D. P. 2012, *ApJL*, **761**, L28
 Pilbratt, G. L., Riedinger, J. R., Passvogel, T., et al. 2010, *A&A*, **518**, L1
 Pineda, J. L., Fischer, C., Kapala, M., et al. 2018, *ApJL*, **869**, L30
 Pineda, J. L., Stutzki, J., Buchbender, C., et al. 2020, *ApJ*, in press (arXiv:2008.01745)
 Planck Collaboration, Ade, P. A. R., Aghanim, N., et al. 2015, *A&A*, **576**, A104
 Planck Collaboration, Aghanim, N., Akrami, Y., et al. 2018, arXiv:1807.06212
 Planck Collaboration, Aghanim, N., Alves, M. I. R., et al. 2016, *A&A*, **596**, A105
 Puerari, I., Elmegreen, B. G., & Block, D. L. 2014, *AJ*, **148**, 133
 Querejeta, M., Schinnerer, E., García-Burillo, S., et al. 2016, *A&A*, **593**, A118
 Rand, R. J., Kulkarni, S. R., & Rice, W. 1992, *ApJ*, **390**, 66
 Sadavoy, S. I., Di Francesco, J., Johnstone, D., et al. 2013, *ApJ*, **767**, 126
 Santos, F. P., Chuss, D. T., Dowell, C. D., et al. 2019, *ApJ*, **882**, 113
 Scarrott, S. M., & Draper, P. W. 1996, *MNRAS*, **278**, 519
 Scarrott, S. M., Ward-Thompson, D., & Warren-Smith, R. F. 1987, *MNRAS*, **224**, 299
 Schinnerer, E., Meidt, S. E., Colombo, D., et al. 2017, *ApJ*, **836**, 62
 Seifried, D., Walch, S., Reissl, S., et al. 2019, *MNRAS*, **482**, 2697
 Seigar, M. S., & James, P. A. 1998, *MNRAS*, **299**, 685
 Seon, K.-i. 2018, *ApJ*, **862**, 87
 Serkowski, K., Mathewson, D. S., & Ford, V. L. 1975, *ApJ*, **196**, 261
 Shetty, R., Vogel, S. N., Ostriker, E. C., & Teuben, P. J. 2007, *ApJ*, **665**, 1138
 Smith, B. J., Struck, C., Hancock, M., et al. 2007, *AJ*, **133**, 791
 Sofue, Y., Nakai, N., & Handa, T. 1987, *PASJ*, **39**, 47
 Sparks, W. B., & Axon, D. J. 1999, *PASP*, **111**, 1298
 Stephens, I. W., Looney, L. W., Dowell, C. D., et al. 2011, *ApJ*, **728**, 99
 Sukumar, S., & Allen, R. J. 1991, *ApJ*, **382**, 100
 Tonry, J. L., Dressler, A., Blakeslee, J. P., et al. 2001, *ApJ*, **546**, 681
 Tritsis, A., Panopoulou, G. V., Mouschovias, T. C., et al. 2015, *MNRAS*, **451**, 4384
 Tully, R. B. 1974, *ApJS*, **27**, 449
 Wardle, J. F. C., & Kronberg, P. P. 1974, *ApJ*, **194**, 249
 Woo, J.-H., & Urry, C. M. 2002, *ApJ*, **579**, 530
 Wood, K., & Jones, T. J. 1997, *AJ*, **114**, 1405
 Xu, S., & Lazarian, A. 2016, *ApJ*, **833**, 215
 Zweibel, E. G., & Heiles, C. 1997, *Natur*, **385**, 131